This is a preprint, the final version is subject to change, of the American Mineralogist (MSA)
Cite as Authors (Year) Title. American Mineralogist, in press.
DOI: http://dx.doi.org/10.2138/am-2018-6238

Revision 2

Visible, Near-Infrared and Mid-Infrared Spectral Characterization of Hawaiian Fumarolic Alteration near Kilauea's December 1974 Flow: Implications for Spectral Discrimination of Alteration Environments on Mars

Marcella Yant[1]*, Kelsey E. Young[2], A. Deanne Rogers[1], Amy C. McAdam[2], Jacob E. Bleacher[2], Janice L. Bishop[3], and Stanley A. Mertzman[4].

[1]Department of Geosciences, Stony Brook University, Stony Brook, New York, USA.

[2]NASA Goddard Space Flight Center, Greenbelt, Maryland, USA.

[3]SETI Institute, Mountain View, California, USA.

[4]Franklin & Marshall College, Earth & Environmental Department, Lancaster, Pennsylvania, USA.

*Marcella.Yant@stonybrook.edu

Abstract:

The December 1974 flow in the SW rift zone at Kilauea Volcano, Hawaii, has been established as a Mars analog due to its physical, chemical, and morphological properties, as well as its interaction with the outgassing plume from the primary Kilauea caldera. We focus on a solfatara site that consists of hydrothermally-altered basalt and alteration products deposited in and around a passively degassing volcanic vent situated directly adjacent to the December 1974 flow on its northwest side. Reflectance spectra are acquired in the visible/near-infrared (VNIR) region and emission spectra in the mid-infrared (MIR) range in order to better understand the spectral properties of hydrothermally altered materials. The VNIR signatures are consistent with silica, Fe-oxides, and sulfates (Ca, Fe). Primarily silica-dominated spectral signatures are observed in the MIR and changes in spectral features between samples appear to be driven by grain size effects in

this wavelength range. The nature of the sample coating and the thermal emission signatures exhibit variations that may be correlated with distance from the vent. Chemical analyses indicate that most surfaces are characterized by silica-rich material, Fe-oxides, and sulfates (Ca, Fe). The silica and Fe-oxide-dominated MIR/VNIR spectral signatures exhibited by the hydrothermally-altered material in this study are distinct from the sulfate-dominated spectral signatures exhibited by previously studied low-temperature aqueous acid-sulfate weathered basaltic glass. This likely reflects a difference in open vs. closed system weathering, where mobile cations are removed from the altered surfaces in the fumarolic setting. This work provides a unique infrared spectral library that includes Martian analog materials that were altered in an active terrestrial solfatara (hydrothermal) setting. Hydrothermal environments are of particular interest as they potentially indicate habitable conditions. Key constraints on the habitability and astrobiological potential of ancient aqueous environments are provided through detection and interpretation of secondary mineral assemblages; thus, spectral detection of fumarolic alteration assemblages observed from this study on Mars would suggest a region that could have hosted a habitable environment.

1. Introduction:

The Martian surface has a complex history that includes volcanic activity and widespread aqueous alteration (e.g., *Bell et al.,* 2008), likely including hydrothermal environments. Hydrothermal environments are of particular interest as they potentially indicate habitable conditions, due to their ability to provide microbial communities with water and energy in an otherwise cold/arid environment (e.g., *Costello et al.,* 2009). On Earth, fumarolic activity can support microbial life including mat-like photoautotrophic communities (e.g., mosses and liverworts) (*Costello et al.,* 2009), autotrophic communities (e.g., mosses, liverworts, algae, fungi, lichens) (*Halloy*, 1991), and halophilic *Archaea* (single-celled microorganisms) (*Ellis et*

al., 2008). Thus, detection of fumarolic environments on Mars would suggest a region that could have hosted a habitable environment.

Key constraints on the habitability and astrobiological potential of ancient aqueous environments are provided through detection and interpretation of secondary mineral assemblages, which vary with alteration conditions (e.g., temperature, pH, fluid-to-rock ratio). Alteration assemblages that were potentially derived from hydrothermal systems have been detected *in situ* on Mars at Gusev Crater and Meridiani Planum (e.g., *Squyres et al.,* 2007; *McCollom and Hynek,* 2005; *Schmidt et al.,* 2008; *Yen et al.,* 2008; *Squryes et al.,* 2012; *Arvidson et al.,* 2014). The search for hydrothermal systems on Mars has been extended to other locations using orbital measurements of reflectance and emission spectra, which are sensitive to mineral species and abundance. For example, detections of silica from orbit have been used to identify potential fumarolic or near-surface hydrothermal activity (e.g., *Bishop et al.,* 2008; *Milliken et al.,* 2008; *Ehlmann et al.,* 2009; *Skok et al.,* 2010; *Marzo et al.,* 2010; *Wray et al.,* 2011; *Smith and Bandfield,* 2012). However, orbital spectral interpretations benefit from comparable spectral studies of analog surfaces as demonstrated in **Table 1** and of samples altered under controlled conditions in the laboratory (e.g., *Yant et al.,*2016) because infrared spectra are also sensitive to other factors, such as particle size, host rock mineral assemblage, and other physical properties. Alteration products often form as a thin coating/fracture fill, or are fine-grained and poorly consolidated, which can lead to challenges in comparing data from different techniques due to non-linear spectral mixing from coating and rind geometry and differences in how the measurements are performed (e.g., *Kraft et al.,* 2003; *Michalski et al.,* 2006; *Kraft et al.,* 2007; *Hamilton et al.,* 2008; *Rampe et al.,* 2009).

Altered ash and tephra sites from the Kilauea region on the big island of Hawaii have been established as Mars analogs due to the physical, chemical, and morphological properties of the

Kilauea eruptive products and a range of potentially Mars-relevant environments (e.g., studies in **Table 1**). For example, chemically altered Kilauea basaltic materials contain secondary minerals and mineraloids (e.g., hematite, Mg/Fe-sulfates, silica) that have been observed on Mars (e.g., *Morris et al.,* 2000a; *Morris et al.,* 2005). Here, we focus on a hydrothermal solfatara site situated on the Kilauea caldera, directly adjacent to the December 1974 flow on its northwest side, and just above the ash outcrop investigated previously (*Bishop et al.,* 2005a). This area provides samples of hydrothermally-altered basalt and alteration products deposited in and around a passively degassing volcanic vent. These samples provide potential spectral analogs to hydrothermally altered regions on Mars.

Earlier studies have characterized the alteration minerals, pathways of high and low temperature weathering, and hydrothermal activity associated with Hawaiian materials (e.g., *Crisp et al.,* 1990; *Morris et al.,* 2000a; *Morris et al.,* 2000b; *Schiffman et al.,* 2000; *Schiffman et al*., 2006; *Bishop et al.,* 2007; *Minitti et al.,* 2007; *Hamilton et al.,* 2008; *Chemtob et al.,* 2010; *Seelos et al.,* 2010; *McCanta et al.,* 2014; *Chemtob and Rossman*, 2014) as summarized in **Table 1**. Some of these previous studies have also provided spectral analyses of naturally altered volcanic materials (e.g., *Crisp et al.,* 1990; *Morris et al.,* 2000b; *Schiffman et al.,* 2006; *Bishop et al.,* 2007; *Minitti et al.,* 2007; *Hamilton et al.,* 2008; *Seelos et al.,* 2010) (**Table 1**). The MIR and/or VNIR spectral properties of in situ altered Hawaiian basaltic materials were obtained from widespread locations on samples that included lava flows, tephra, ash, and basalt coatings. Silica was observed in all of these studies, as amorphous silica (*Crisp et al.,* 1990; *Schiffman et al.,* 2006; *Bishop et al.,* 2007; *Seelos et al.,* 2010), nanophase silica (*Morris et al.,* 2000b), or hydrated silica (*Minitti et al.,* 2007). *Hamilton et al.* (2008) detected silica as a mineral phase, cristobalite. Another common phase among these studies is Fe-oxides, which were identified by all of these works, excluding

Morris et al. (2000b). Sulfates (Na-Al, Ca, Fe) were also observed in majority of these previous studies. Phyllosilicates were only exhibited in two of the sample groups (*Bishop et al.,* 2007; *Hamilton et al.,* 2008).

A previous study by Seelos *et al.* (2010) included samples and remote measurements from the same fumarole studied here, thus we describe their results in more detail. This particular fumarole is of interest because it is young and well-preserved, and large enough to be analyzed from aerial and orbital observations. Reflectance data of basalts in the Ka'u desert of Hawaii were collected using an Airborne Visible Near Infrared Imaging Spectrometer in order to identify the mineralogic components of relatively young basaltic material. Most of the studied area had spectral signatures consistent with the presence of ferrous and ferric iron in such minerals as pyroxene, olivine, hematite, goethite, and poorly crystalline iron oxides or glass. However, ash duricrusts, coatings on the youngest lava flows, and surfaces downwind of the solfatara vents, exhibited a spectral feature near 2.25μm, associated with opaline silica. The hydrothermally altered solfatara material was spectrally dominated by sulfur and hydrated silica (*Seelos et al.,* 2010).

The naturally-altered fumarolic materials analyzed here are compared in this study with assemblages formed on laboratory-altered synthetic Martian materials from *Yant et al.* (2016). These previously studied synthetic basaltic glasses represent one type of environment predicted to be common on Mars, acid sulfate weathering under low fluid-to-rock ratios and nearly isochemical conditions (*Burns and Fisher*, 1990; *Bigham and Nordstrom*, 2000; *Madden et al.,* 2004; *Golden et al.,* 2005; *Ming et al.,* 2006). Results from *Hurowitz and Fischer* (2014) indicate that the chemistry of soils at Gusev crater and Meridiani Planum and rinds at Gusev crater suggest a water limited environment with chemical alteration dominated by sulfur-rich fluids; this resulted in the formation of secondary phases without physical separation from the primary substrate, also

117 referred to as "cation-conservative" (*Niles and Michalski,* 2009) conditions. The cation-
118 conservative chemical weathering characteristics displayed by the undisturbed soils from Gusev
119 crater and Meridiani Planum indicate similar weathering processes for the alteration rinds on rocks
120 and the regolith on Mars (*Hurowitz and Fischer,* 2014). Here we investigate how the chemical and
121 spectral properties of naturally-altered Hawaiian fumarolic deposits compare with those of
122 alteration assemblages formed in other Mars-relevant environments.

123 In this study, we extend the earlier work through VNIR and MIR spectral characterization
124 of the altered glassy basalt surrounding a fumarole vent adjacent to the December 1974 Kilauea
125 flow. This spectral characterization will enhance the understanding of the spectral properties of
126 alteration products found in hydrothermal systems. In addition, analytical measurements including
127 X-ray fluorescence (XRF), X-ray diffraction (XRD), and scanning electron microscopy (SEM) are
128 coordinated with spectral measurements in order to bridge the gap between alteration assemblages
129 and infrared signals. Specifically, we address the following questions: 1) What are the VNIR and
130 MIR spectral characteristics of fumarolic alteration from basaltic starting materials? 2) How do
131 the infrared spectral signatures relate to chemical and physical variations among samples? 3) How
132 do MIR spectral signatures compare with VNIR signatures? 4) How do the spectral properties of
133 fumarolic deposits compare with those of alteration assemblages formed in other Mars-relevant
134 environments?

135 **2. Methods:**

136 **2.1 Sample Collection:**

137 We collected samples in June 2015 from an active solfatara site, situated directly adjacent
138 to the December 1974 flow at Kilauea caldera (19.362403° N, -155.311090° W), on its northwest
139 side (**Figure 1**). This site consisted of hydrothermally altered basalt and alteration products

deposited in and around a passively degassing fumarole vent. For the samples with "HI_15_MHY" designations, material was collected within 19.5m of the main volcanic vent with the lowest sample number corresponding with the furthest location. The samples with "HI_15_Solf" designations were collected from the top and sides of the ridge. The "HI_15" portion of the samples names are not included for labels on figures to cut down on length. The collected material (**Figure 1, Table 2)** consisted of altered basaltic rocks with variously colored coatings (blue, yellow, white), coatings on friable, wet reddish ash, as well as one lag deposit sample with centimeter sized white and yellow grains. Samples were chosen to reflect the wide variety of different coatings found at this site. Samples were carefully removed from their locations and best efforts were made to preserve the samples in their original form.

2.2 Analytical Techniques:

The samples were spectrally characterized using VNIR and MIR spectroscopy; analyses were performed on the sample surfaces as collected (e.g., as solid surfaces instead of powdered samples). VNIR (350-2500nm) bidirectional reflectance spectra were acquired using an ASD FieldSpec3 Max spectrometer at Stony Brook University under ambient laboratory conditions. The samples were purged overnight to remove H_2O and CO_2 from the air and measurements were taken under purged conditions. This was done to remove the spectral effects from adsorbed water on the sample surfaces (e.g., *Anderson and Wickersheim,* 1964). The purged spectra were compared with previously collected measurements that were performed without an overnight purge. Distinct differences were observed between the two data sets, with adsorbed water broadening the absorption features near 1.4 and 1.9μm. The purged spectra provided more diagnostic signatures and these spectra are provided in **Figure 2**. The measurements were collected with incidence and emergence angles of 30° and 0°, respectively. The measurements were performed relative to

163 Spectralon and then corrected for the reflectance properties of Spectralon. VNIR spectra were
164 compared with library spectra of well-characterized samples available from RELAB
165 (http://www.planetary.brown.edu/relab/).

166 MIR emissivity spectra were acquired between 225-2000 cm^{-1} on Stony Brook
167 University's Nicolet 6700 FTIR spectrometer equipped with a CsI beamsplitter and deuterated
168 triglycine sulfate cesium iodide (DTGS CsI) detector. The atmosphere was purged of H_2O and
169 CO_2. Each sample was put into an aluminum sample cup painted with Krylon Ultra Flat Black
170 paint in order to minimize spectral contributions from the sample cups. Measurement of thermal
171 emission spectra requires that the samples be at a different temperature than the detector; typically,
172 samples are heated above ambient temperature to achieve this requirement (e.g. *Ruff and*
173 *Christensen*, 1997). However, because our samples were expected to contain sulfate minerals,
174 which could dehydrate upon heating, emission measurements of altered samples were performed
175 by cooling the samples well below the detector temperature (*Baldridge and Christensen*, 2009). A
176 thermo-electric cooling apparatus was used to actively cool the samples during spectral
177 measurement. The samples were cooled to approximately -15°C within the chamber and
178 maintained at that temperature for the duration of 256 scans (~9 minute integration).

179 MIR spectra of altered samples were analyzed using linear least squares analysis (e.g.,
180 *Ramsey and Christensen*, 1998; *Rogers and Aharonson*, 2008) with a library of sulfate, silica, Fe-
181 oxide, clay, and sulfur spectra, over the spectral range of 400-1400 cm^{-1}. Most of the library spectra
182 and samples used in this study are described in *Christensen et al.* (2000); *Wyatt et al.* (2001),
183 *Glotch et al.* (2004), *Lane et al.* (2007), *Glotch and Kraft* (2008), *Baldridge* (2008), *Ruff et al.*
184 (2011), *Lane et al.* (2015), and *Sklute* (2015) (**Supplementary Table 1**). A quasi-linear slope
185 spectrum was also included to account for slopes present in the altered samples, due to spatial

and/or temporal non-isothermalities within the sample or sample collection process from temperature fluctuations. Although linear spectral mixing cannot be assumed for some of these mixtures, the models allow us to characterize the spectrally dominant phases for descriptive purposes (e.g., sulfate- or silica-dominated assemblages), and provides a comparison to what would be observed in models of spectra acquired from Mars.

Chemical and morphological analyses of secondary phases were obtained using a LEO 1550 SFEG scanning electron microscope (SEM) equipped with an EDAX energy dispersive X-ray spectrometer (EDS). SEM analyses were only acquired for the HI_15_MHY samples. Analyses were performed using an accelerating voltage of 20kV. The EDS system is capable of quantitative elemental analysis, but only for relatively flat surfaces. All of the EDS analyses discussed here are semi-quantitative because the analyses were performed on samples with variable surface angles. The EDS analyses do not allow for exact element ratios, but they do provide the elemental composition of the material. With the ratios provided by EDS, a comparison between elements present in the spectra can be done. Combining the elemental makeup and the morphology of a grain can allow for mineral identification. The other analytical techniques (XRF, XRD) can also be utilized to properly identify phases.

X-ray diffraction patterns were determined for a suite of samples using a PANalytical X'Pert PRO X-ray diffractometer equipped with a 15-position sample changer and a ceramic Cu X-ray tube at Franklin and Marshall College. Small aliquots of each sample were hand ground using a ceramic mortar and pestle. Each finely powdered sample was mounted on zero background plates and analyzed sequentially on the same day at 45 kV and 40 mA with the sample holder rotating at 4 revolutions per second while being analyzed to insure sample homogeneity. Scans from 6° to 70° 2θ were made for each sample. Routine identification of crystalline materials is made using

PANalytical, Inc. Highscore software, which is compatible with the International Center for Diffraction Data (ICDD) Database. Readily visible on each diffractogram is a hump in the background intensity located between approximately 15° and 35° 2θ that varies in intensity and is related to the amount of amorphous material present in each sample.

Though initially developed for use in industry and mining, the handheld X-ray fluorescence (hXRF) has now been established as a viable and valuable technology for *in situ* geochemical analysis (*Young et al., 2015*). Though laboratory XRF instruments will remain the gold standard for detailed chemical analyses, the hXRF permits *in situ* analyses, which are advantageous in this case as they can analyze thin coatings on samples that can be hard to isolate from their underlying bulk rock. As this study seeks to examine thin coatings and veneers in the solfatara region, hXRF technology provides a valuable way to analyze coatings in a large number of locations throughout the study area. Due to the heterogeneous nature of the samples in this study, we focus on measuring the coating materials. *Young et al.* (2011, 2012) demonstrated that the hXRF can provide reasonable constraints on the chemistry of basaltic rocks, and we therefore use this technology in this study. The samples were analyzed using an Olympus Innov-X DELTA Premium Handheld XRF Analyzer. The hXRF calibrations were done using standards (Samples CP-5, HWHL100, BPNTX1, WIME101, and TMGNV5) and the errors on these measurements range from a couple of wt. % to ~10 wt. % depending on the element. All of the calibration curves and methodologies are outlined in *Young et al.* (2016). The XRF data was separated into groups based on chemical similarities determined using a minimum distance clustering algorithm. The chemical abundances for each sample are treated as 8-dimensional vectors. Similarities between vectors were determined by calculating the euclidean distances between pairs of vectors. Two samples separated by small distances are chemically similar, whereas samples separated by large distances are

dissimilar. The euclidean distances between all samples were plotted and natural breaks between distance values were used to define the three chemical groups shown in **Figure 6**.

3. Results:

3.1: Infrared Spectroscopy

An overview of the alteration material observed for each sample is shown in **Table 2**. The thermal emission spectra were first separated into groups based on variations in spectral properties (**Figure 2a-d**). Most of the thermal infrared spectra of our samples appear to be dominated by silica (**Figure 2a**), exhibiting features consistent with silica sinter, microporous silica, and/or amorphous silica (*Ruff et al.,* 2011). Within the silica dominated group (Group 1), there are 4 sub-groups. The first sub-group (1-1) exhibits deep silica features near 1240, 1100, and 470 cm^{-1}. The second sub-group (1-2) displays a shallowing of these three features, whereas in the third sub-group (1-3) the feature near 1240 cm^{-1} is severely shallowed. The fourth sub-group (1-4) exhibits silica features that are shifted when compared to the previous groups, from 1240 and 1100 cm^{-1} to 1260 and 1115 cm^{-1}, respectively. The remaining 3 groups each only have one associated signature. Group 2 exhibits features near 1145, 675, and 600 cm^{-1} suggesting a Ca-sulfate (gypsum)-dominated (*Bishop et al.,* 2014) assemblage (**Figure 2b**). The next group is most consistent with Fe^{+3}-sulfate (coquimbite) with absorptions near 1170, 1095, 525, and 470 cm^{-1} (*Lane et al.,* 2015), but as will be described below, is also consistent with a fine-grained mixture of silica, Ca-sulfate, and Al-sulfate (**Figure 2c**). Silica and Fe-oxide (hematite) influence the spectra for the last group with features near 1250, 1105, 655, and 470 cm^{-1} (**Figure 2d**).

The reflectance spectra are divided based on the previous groups established for the MIR emission spectra (**Figure 2e-h**). Features consistent with silica ($SiO_2 \cdot nH_2O$) are observed for all of the samples in the VNIR (near 0.98, 1.19, 1.45, 1.93 and/or 2.25μm (*Goryniuk et al.,* 2004; *Rice*

et al., 2013)), but some samples exhibit additional features influenced by Fe-oxides (features 0.6< μm (e.g. *Morris et al.,* 1985; *Bishop and Murad,* 1996)) and/or sulfates (1.4-1.5, 1.75-1.85, 1.9-2.0, ~2.2 and/or ~2.4 μm (*Bishop et al.,* 2005b; *Lichtenberg et al.,* 2010; *Lane et al.,* 2015; *Cloutis et al.,* 2006) (**Table 2**). Opal-CT and silicic acid are referred to here as hydrated silica as they both represent $SiO_2 \cdot nH_2O$ and SiOH species (*Rice et al.,* 2013). Opal-CT is identified by characteristic features near 1.4-1.41 and 1.91 μm, along with a broader band centered at 2.21 μm with a shoulder extending towards 2.25μm (e.g. *Anderson and Wickersheim,* 1964; *Milliken et al.,* 2008; *McKeown et al.,* 2011). Additionally, silicic acid (synthetic silicon dioxide, a white solid powder formed by the acidification of silicate salts (e.g., sodium silicate) in aqueous solution) was used to identify hydrated silica with spectral features near 0.98, 1.19, 1.45, 1.93μm (*Rice et al.,* 2013). These features are characteristic of H_2O in several minerals, however, based on the shape of the features near 0.98, 1.19, 1.4, and 1.9μm, these spectral bands may indicate the presence of hydrated silica in our samples.

In general, the features present in the reflectance spectra are similar within the groups of samples, however there are some variations. In Group 1-1, the spectra exhibited deep silica features in the MIR. Although influence from silica is observed for all five samples in the VNIR, a broad absorption in the 0.92-1.06μm range is also exhibited, consistent with Fe^{+2}-sulfate (melanterite) and/or Fe-oxide (akaganéite), or perhaps an iron impurity within the silica phase or mineral mixing (**Figure 2e**). The shoulder near 0.53μm observed for HI_15_MHY_001 and Solf_002_1 may also indicate influence from Fe-oxides. Overall, MHY_001, Solf_001_1, and Solf_002_1 display shallow features consistent with basaltic glass along with some influence from opal-CT near 1.91 and 2.25μm; whereas MHY_002a and MHY_002b exhibit deeper features primarily consistent with opal-CT. Additionally, MHY_001 and Solf_002_1 exhibit negative spectral slopes and a

concave nature, possibly due to thin coatings and/or fine grain size (e.g., *Fischer and Pieters*, 1993; *Brown et al.,* 2014) or due to acidic leaching of glass (*Horgan and Bell,* 2012). Group 1-2 exhibited shallowed silica features in the MIR. Again all of the VNIR spectra in this group are consistent with the presence of silica, however all of these samples also exhibit influence from Fe-oxide (akaganéite) and/or trace iron impurity, near 0.44, 0.53 and/or 0.98µm (**Figure 2e**). The feature near 0.44 could also be due to the presence of Fe^{+2}-sulfate (melanterite) and/or Fe^{+3}-sulfate (copiapite or jarosite). The features observed near 1.45, 1.91, and 2.25µm for the samples in this group are consistent with opal-CT.

The MIR signatures for Group 1-3 were silica-dominated, but with severe shallowing of the 1240 cm^{-1} feature. The VNIR signatures for both samples in this group are influenced by silica, exhibiting features consistent with opal-CT (1.45, 1.91, 2.25µm) (**Figure 2e**). Both samples included in this group also display features that may be due to the presence of Fe-oxide (akaganéite), near 0.53 and 0.98µm. The shifted silica features observed for Group 1-4 in the MIR correspond with a VNIR signature dominated by silica and Ca-sulfate (**Figure 2e**). The shape of the feature near 1.45µm is most consistent with Ca-sulfate (gypsum) along with the absorption near 1.76µm. The feature near 2.25µm is most consistent with opal-CT. Group 2 is Ca-sulfate-dominated in the MIR, and exhibits features dominated by Ca sulfate (gypsum, near 1.45, 1.76, 1.94µm) with some influence from silica near 2.25µm and silicic acid near 0.98 and 1.19µm (**Figure 2f**). The reflectance features of the Group 3 spectrum are consistent with Ca-sulfate (gypsum or bassanite, near 1.45, 1.93µm) in the VNIR with opal likely as well due to the broadness of these bands, lack of 1.76µm feature, and the presence of a feature near 2.25µm (**Figure 2g**). The last group exhibits influence from silica and Fe-oxide in the MIR. The reflectance signature for Group 4 is also consistent with adsorbed water bands observed for hydrated silica (1.16, 1.45,

1.76, 1.93μm) and Fe-oxide (near 0.96μm). Akaganéite provided the best match from the Fe-oxide library spectra used in this study, as it contains characteristic Fe^{+3} absorptions near 0.44, 0.59 (shoulder), and 0.92μm (*Bishop et al.,* 2015); however, we did not observe the expected H_2O band near 1.95-2.0μm or OH band near 2.46μm, so akaganéite cannot be a dominant component. This sample also may display influence from Fe^{+2}-sulfate (melanterite) and/or Fe^{+3}-sulfate (copiapite, jarosite) near 0.44 μm (**Figure 2h**).

Linear least squares analysis was used to model the averaged thermal emission spectra for each group. A full table of the modeling results is available in the Supplementary Material (**SI 1**). The phases listed as minor are below the detection limits of this method and may not be present. The MIR Group 1-1 also had a silica-dominated modeled assemblage, but lower amounts of sulfate and minor Fe-oxide were used by the model to improve the fit (**Figure 3a**). The shallowed silica features exhibited by MIR Group 1-2 also resulted in a silica-dominated modeled assemblage, but with influence from sulfate, clay (montmorillonite, Fe/Al-smectite), and minor sulfur (**Figure 3b**). The relatively poor fits for Groups 1-3 and 1-4 indicate non-linear mixing likely due to small particle sizes, discussed further in Section 4.1, and poorly crystalline components. An Fe^{+3}-sulfate-Al-sulfate-dominated modeled assemblage (**Figure 3c**) was observed for Group 1-3, contrasting the silica-dominated grouping. The shifted silica features observed for MIR Group 1-4 still produced a silica-dominated modeled assemblage, but with influence from Fe-oxide and sulfur (**Figure 3D**). The modeled spectrum for MIR Group 2 resulted in a Ca-sulfate-dominated assemblage with influence from silica (**Figure 3e**). The Fe^{+3}-sulfate-dominated model fit for MIR Group 3 is relatively poor, as with Groups 1-3 and 1-4 and is likely influenced by particle size effects (**Figure 3f**). Last, the modeled assemblage for the MIR Group 4 is dominated by silica and

This is a preprint, the final version is subject to change, of the American Mineralogist (MSA)
Cite as Authors (Year) Title. American Mineralogist, in press.
DOI: http://dx.doi.org/10.2138/am-2018-6238

Fe-oxide with influence from sulfate (**Figure 3g**), consistent with the silica/Fe-oxide-dominated grouping.

3.2 Chemical and Mineralogical Analyses

SEM analyses were only acquired for the HI_15_MHY samples and thus only these samples are discussed (no data was collected for Group 1-3 or Group 3) using secondary electron images. The Group 1-1 samples all exhibit similar silica-dominated surfaces (**Figure 4a-c).** The surface of HI_15_MHY_001 is characterized by a Si-rich leached coating, overlying a glass with considerable Al, Ca, Mg, and Fe (**Figure 4a**). HI_15_MHY_002a is also dominated by a Si-rich coating (**Figure 4b**), with some Fe-sulfates and Ca-sulfates observed sparsely. A Si-Ti-Fe-rich surface coating is also observed, but is not as pervasive as the Si-rich surface. A Si-rich surface is also observed for HI_15_MHY_002b, overlying a glass similar to that observed for HI_15_MHY_001 (**Figure 4c**). The samples from Group 1-2 also exhibit a Si-rich coating, but are consistent with other materials (**Figure 4d-e**). HI_15_MHY_003 has a Si-rich surface, with Ca-sulfate present in some areas (**Figure 4d**). HI_15_MHY_005 has a Si-rich surface with Fe-Ti-oxides and Ca-sulfate deposited on top (**Figure 4e**). The surface of the only sample from Group 1-4, HI_15_MHY_007a, is characterized by Si-rich material and Ca-sulfate (**Figure 4f).** With Group 2, the surfaces are less dominated by silica compared to Group 1. HI_15_MHY_007b exhibits centimeter sized clasts of Si-rich material (**Figure 4g**) and Ca-sulfates (**Figure 4h**). For Group 4, the surface of HI_15_MHY_006 is characterized by Si-rich material overlain considerably by Fe-Ti-oxides (**Figure 4i**).

The results from the XRD analyses are listed in **Table 2.** Generally, amorphous material +/- crystalline silica was observed for all of these samples. The amorphous material could indicate glass, silica, allophane, imogolite, or other amorphous materials which result in a characteristic

346 hump in the XRD pattern. Crystalline silica is referring to crystalline polymorphs of SiO_2 (e. g.,
347 tridymite, cristobalite) which have distinct XRD peaks. Small amounts of additional phases were
348 observed for Group 1-2 (blixite, Fe-oxides, zeolites, K-sulfate), Group 1-3 (Fe-oxides), and Group
349 2 (Ca-sulfate, sulfur). The XRD patterns for all of these samples exhibited broad features
350 consistent with an amorphous material such as amorphous silica, allophane and/or basaltic glass.
351 For three samples, the broad diffraction hump had a width of ~16 °2θ and the center was shifted
352 to lower °2θ values (~23 °2θ), indicating material that is more Si rich than pure basaltic glass
353 (**Figure 5**). No halite was observed in these samples.

354 The XRF data has been separated into 3 groups based on chemical similarities determined
355 using a minimum distance clustering algorithm on handheld XRF chemical data for each sample
356 (**Figure 6A**). This independent XRF-based grouping was done in order to compare how/if element-
357 based compositional variability corresponds with spectrally-determined variability. Chemical
358 variations are most strongly driven by abundances of Si, Fe, and less so by Al and Ca. The
359 abundance of Si is negatively correlated with Fe, Al, and Ca. The XRF Group 1 consists of
360 samples HI_15_Solf_002_3 (MIR Group 1-3) and HI_15_Solf_003_2 (MIR Group 1-2) and
361 displays relatively higher enrichment in Si and lower enrichment in Ca and Fe compared to the
362 other groups. XRF Group 2 exhibits medium enrichment in Si, Fe, Al, and Ca and includes
363 samples from MIR Group 1-1 (HI_15_MHY_001, HI_15_MHY_002a), Group 1-2
364 (HI_15_MHY_003, HI_15_MHY_005, HI_15_Solf_003_3), Group 1-4 (HI_15_MHY_007a),
365 and Group 4 (HI_15_MHY_006). The XRF Group 3 includes samples from MIR Group 1-1
366 (HI_15_Solf_001_1, HI_15_Solf_002_1), Group 1-3 (HI_15_Solf_001_2), and Group 3
367 (HI_15_Solf_002_2) which display relatively low enrichment in Si, and high enrichment in Al,
368 Ca, and Fe. The Al vs. Si and Fe vs. Si plots (**Figure 6B-C**) display the negative correlations that

were observed by the minimum distance clustering. These plots also indicate that the XRF compositional groupings of samples are not the same as the previous MIR groups, although there are some similarities.

4. Discussion

4.1 Spectral Detectability

Overall, the surfaces of the hydrothermally altered samples analyzed here are characterized by silica-rich material +/- Fe-oxides and Ca-sulfate, based on chemical and mineralogical analyses (**Table 2**). Several XRD patterns exhibited amorphous humps centered near 24 2θ; this position is consistent with an amorphous material that is more Si rich than basaltic glass (**Figure 5**). Silica-rich materials generally have a narrower hump centered at lower positions near 25 2θ, whereas basaltic glass generally has a broader hump centered at higher positions, near 31 2θ, (*Morris et al.,* 2015). This is consistent with MIR/VNIR data that showed amorphous silica contributed to the spectral shape for all samples. Although both the MIR/VNIR and handheld XRF data are detecting strong enrichments in Si or Si-bearing phases, compositional groupings of samples using each technique are not well correlated. This could be due to the sensitivity of the handheld XRF to chemical changes versus MIR/VNIR spectroscopy which are sensitive to mineral species and abundance. Likewise, minor alteration phases observed on sample surfaces in SEM images are often not exhibited in the XRD data due to the small contribution of the surface material to the bulk sample.

In general, the dominant surface phases are clearly identified in the VNIR and MIR spectral signatures; however, for some samples, the spectral models include large abundances of phases that are absent in SEM data. For example, the surfaces of samples HI_15_MHY_001 and HI_15_MHY_002b (Group 1-1) are both characterized by a silica coating based on SEM analysis

392 (**Figure 4a,c**). However, in the MIR additional phases (sulfates and Fe-oxides) are needed in order
393 to provide the best fit to the sample spectra (**Figure 3a**). In addition, phyllosilicates
394 (montmorillonite, Fe/Al-smectite) are included in the modeled assemblage for Group 1-2 (**Figure**
395 **3b**) when none was observed on any of the sample surfaces. This phenomenon, as well as the poor
396 fits to some of the modeled spectra (e.g., MIR Group 3), are likely due to the fine-grained nature
397 of the weathered surfaces. Volume scattering and transmission through small grains or thin
398 coatings can give rise to spectral features that are not well modeled by library spectra of pure,
399 coarse-grained phases.

400 Differences in grain size also appear to be a major factor in the spectral differences between
401 the samples in the MIR silica-dominated group (Group 1). SEM data was only collected for the
402 HI_15_MHY samples and thus only these samples are discussed. The samples with the deepest
403 features (Group 1-1; HI_15_MHY_001, 002a, and 002b) all have continuous silica coatings with
404 little to no fine-grained surface material (**Figure 4a-c**). However, the samples with shallow silica
405 features (Group 1-2, 1-4; HI_15_MHY_003, 005, 007a) have finer-grained surfaces (**Figure 4d-**
406 **f**), and HI_15_MHY_005 and HI_15_MHY_007a also have numerous cavities. Additionally, the
407 shallow silica features could be due to a relatively low abundance of silica-rich material due the
408 presence of oxides and sulfates.

409 The variations observed between the subgroups of the silica-dominated thermal emission
410 spectra appear to be correlated with distance from the volcanic vent. The distance was only
411 measured for the HI_15_MHY samples and thus only these are discussed. The purest silica features
412 were exhibited by the material farthest from the vent (Group 1-1, 19.0 – 18.0m) with shallowing
413 of silica features in the intermediate material (Group 1-2, 11.5m – 4.7m), and shifting of features
414 in the material closer to the vent (Group 1-4, 4.5m). The material collected closest to the vent

exhibited sulfate-dominated features (Group 2, 4.5m and Group 3, 4.0m). Unfortunately, no fluid or gas measurements were available, and interpretation of the influence of changing gas composition cannot be determined at this time. The presence of sulfates could be due to a greater supply of sulfur near the vent, contributing to the formation of sulfates in the material closest to the vent or due to easier removal of mobile cations farther from the vent. The nature of the sample coating also appears to change with distance from the vent. Materials that exhibit leached surfaces are observed farther away from the vent (Group 1-1, 19.5 – 18.0 m, **Figure 1b-c**) and may represent passive silica enrichment from removal of other elements during weathering (e.g., *Morris et al.,* 2008; *Yen et al.,* 2008). Generally, thicker silica encrustations are observed on samples located closer to the vent (Groups 1-2, 1-3, 1-4, 2, 3, and 4, 11.5 – 4.0 m, **Figure 1d-i**) and may partially result from silica precipitated during low water-to-rock aqueous alteration of the basalts by acidic aerosols supplied by the vent (e.g., *Ruff et al.,* 2011). Furthermore, the shift of the silica feature from 1115cm^{-1} to 1100cm^{-1} observed in the Group 1-4 MIR spectra could be due to Al-substitution for Si. This could be expected in the samples observed here, as Al (along with Si and Fe^{+3}) has increased solubility under acidic conditions (*Hurowitz et al.,* 2006).

Many of the samples exhibited low abundances of Fe-oxides and sulfates in addition to silica in the chemical analyses (HI_15_MHY_002a, 003, 005, 006, 007a, 007b, HI_15_Solf_003_3, **Table 2**). Although these low-abundance materials were not easily identifiable in many of the MIR signatures (**Figure 2**) they were commonly distinguished in the VNIR range. The differences observed between the MIR and VNIR signatures are attributed to differences in mineral transparency between these two techniques and the nature of the alteration material. Some samples exhibit powdery surfaces that result in multiple surface scattering and reduced restrahlen features in the MIR (*Hunt and Vincent*, 1968; *Salisbury and Wald*, 1992;

438 *Mustard and Hays*, 1997), making it difficult to identify lower abundance phases. In addition, the
439 fine grains and thin coatings that comprise the alteration material permit energy transmission
440 through the grains/coatings (e.g., *Hunt and Logan,* 1972; *Clark and Roush,* 1984). This effect is
441 enhanced in the VNIR due to the lower absorption coefficients in this range and increased
442 importance of volume scattering (*Salisbury and Wald,* 1992). This allows small abundance phases
443 to be more easily detected in the VNIR and these may dominate the spectral properties.

444 The alteration phases observed here provide similar results to the previous works in **Table**
445 **1**. Here we observed MIR signatures dominated by silica and VNIR signatures influenced by silica,
446 sulfate(s), and Fe-oxide(s). The phyllosilicate phases detected by *Golden et al.* (1993), *Morris et*
447 *al.* (2000a), *Schiffman et al.* (2000), *Bishop et al.* (2007), and *Hamilton et al.* (2008) were only
448 observed using linear least squares modeling of the MIR data for Group 1-2 in abundances ≤ 10%.
449 Our results agree with the environmental conditions suggested by *Schiffman et al.* (2000) which
450 attribute the development of opaline crusts to acidic conditions (pH <6) and clay mineral formation
451 to more neutral conditions (pH 6.5 – 7.8).

452 The global abundance and species of chemical alteration products on planetary surfaces
453 are related to the starting composition of unaltered protolith, the style and duration of alteration
454 processes, the fluid composition, the fluid-to-rock ratio (e.g., *Tosca et al.,* 2004; *Golden et al.,*
455 2005; *Ming et al.,* 2006), and ultimately, to the preservation of those products in rocks and soils.
456 Thus, detection and interpretation of alteration mineral assemblages is critical to deciphering the
457 history of the Mars. However, amorphous material often forms as a product from the alteration of
458 volcanic material and can cause difficulty in identifying additional alteration phases and obtaining
459 quantitative abundances of alteration phases. Amorphous phases are an important component on
460 Mars and have been observed in several occurrences by the Chemistry and Mineralogy Instrument

461 (CheMin) onboard Curiosity (e.g., *Bish et al.,* 2013). The presence of amorphous material was
462 determined based on the appearance of a broad, diffuse peak rather than the narrow diagnostic
463 peaks of well crystalline phases. This provides a challenge for identification because these phases
464 lack long-range crystallographic order so analyses that depend on crystal structure (e.g., XRD) are
465 non-unique. The fumarolic materials in this study may provide an analog for some of the
466 amorphous phases on Mars, and the distinctive Si-rich features observed show that the addition of
467 MIR/VNIR data helps to distinguish some of those materials.

468 **4.2 Hydrothermal Alteration on Mars**

469 MIR and VNIR spectral analyses of hydrothermally altered Hawaiian basalts are presented
470 here in order to enhance the understanding of the infrared spectral properties of weathered
471 materials. The spectral shapes of the signatures acquired in this study can be applied to VNIR and
472 MIR spectral data obtained from Mars in order to better constrain variability of weathering on a
473 global scale. Based on our results, silica detections across both wavelength ranges are common
474 from fumarolic alteration. However, we note that silica deposits are not limited to high-temperature
475 and/or fumarolic processes (e.g., *McLennan,* 2003; *McAdam et al.,* 2008). For example, silica can
476 form through acid fog weathering of basalt, with low water-to-rock ratios under near isochemical
477 conditions (*Tosca et al.,* 2004). Based on a number of chemical and mineralogical measurements
478 made by landed missions (*Clark et al.,* 1993; *Haskin et al.,* 2005; *Ming et al.,* 2006; *Clark et al.,*
479 2005; *Morris et al.,* 2006), an acid fog environment has been proposed as a common and persistent
480 alteration setting on the Martian surface (*Hurowitz and McLennan,* 2007; *Hurowitz and Fischer,*
481 2014). Thus, it is useful to compare the spectral properties of silica-bearing samples from this
482 fumarolic environment to those formed in a closed-system acid sulfate environment. Below, we
483 compare the spectral characteristics of our samples to those from a previous study in which basaltic

484 glass was subjected to low-temperature, isochemical weathering under low water-to-rock ratios
485 (*Yant et al.,* 2016).

486 In a previous study, sand-sized synthetic Martian glass particulates were submerged in sulfuric-
487 hydrochloric acidic solutions (pH 0-4) under low fluid-to-rock ratios (1:1) at ambient temperature
488 and pressure (*Yant et al.,* 2016). This system simulates an acid-fog environment which is
489 considered closed due to the very low fluid-to-rock ratios. We use a laboratory environment
490 because of the difficulty in determining how long a natural environment has been closed. In
491 general, acid alteration on particles resulted in sulfate-dominated assemblages in the most acidic
492 solutions (pH≤1) that exhibited well-developed sulfate features, in the MIR, and strong 1.45, 1.95,
493 and 2.40μm features in the VNIR. Amorphous silica was present based on chemical analyses, but
494 not as detectable in the MIR/VNIR spectra. The results from *Yant et al.* (2016) contrast
495 significantly with the silica-dominated assemblages observed for the majority of the samples in
496 this study (**Figure 7**).

497 The likely reason for the observed differences relates to open vs. closed system weathering.
498 Sulfates, Fe-oxides, and silica are commonly identified as alteration products in Martian analog
499 studies (**Table 1**), and when present on the surface of substrates each contributes uniquely to the
500 visual appearance and MIR/VNIR spectral signatures observed for these materials. In closed
501 system weathering, as simulated by *Yant et al.* (2016), small volumes of acidic fluid react with the
502 surface of the material resulting in a fluid enriched in the most soluble elements . A leached
503 alteration rind, depleted in the most soluble elements, is left behind, and the fluid subsequently
504 undergoes evaporation and deposits alteration minerals. Si^{+4} is relatively insoluble in low pH
505 conditions (pH<2-3) and basaltic cations are relatively mobile (e.g., *El-Shamy et al.,* 1972; *Minitti*
506 *et al.,* 2007). This can result in basalt leaching or dissolution that could form a silica-enriched layer

beneath the fluid containing the mobile cations. When the fluid is evaporated, in a closed system, salts containing the more mobile cations can precipitate on top of the silica-enriched layer. The formation of the sulfates overlying the silica layer results in a larger spectral signal from the sulfates relative to the silica. In order to form a sulfate-dominated assemblage, the fluid-to-rock ratio needs to be small enough that the soluble elements are not mobilized and are allowed to precipitate on top of the leached surface in a closed system (*Hurowitz et al.,* 2006). Additionally, sulfates that are precipitated over a diffuse area can be remobilized by dew and/or rain, whereas silica coatings are less soluble and less likely to be removed.

If the system is open and the fluid can migrate, a silica or Fe-oxide-dominated assemblage can be formed (*Dorn*, 2012; *Chemtob and Rossman*, 2014). *Chemtob and Rossman* (2014) describe the formation of silica coatings on glassy basalts from Hawaii through reaction of acidic fluids in an open system using the following model. Fresh rock surfaces are wetted by rainwater or condensed water vapor. The fluid becomes acidified by volcanically derived liquids and reaction with this low pH fluid results in dissolution of the basalt. The basaltic cations are more soluble than the silica and the cations remain dissolved at low pH and the silica is precipitated in place. The fluid is mobilized carrying away the more soluble cations, leaving behind Ti and Fe^{+3}, which have lower mobility and are deposited as Fe-Ti-oxides, in addition to the silica. *Chemtob and Rossman* (2014) suggest that this mobilization is facilitated by liquid water, possibly sourced from rainwater and condensed water vapor from nearby plumes. Silica can also be transported to the surface by fluids that penetrate to the interior of the basalt. As alteration continues over a period of years, episodes of dissolution-reprecipitation can result in the thickening of the silica layer and the remobilization of Fe and Ti to the surface, producing silica or Fe-oxide-dominated spectral signatures like those observed here. Additionally, Al behaves in a manner similar to Fe^{+3} and

exhibits increased solubility in acidic conditions (Hurowitz *et al.,* 2006) and could be expected to precipitate under the conditions shown here. Negative correlations were observed between Fe vs. Si and Al vs. Si in the XRF data (**Figure 6**) supporting the interpretation that Fe and Al are both precipitating on top of the silica layers. The results shown here for the natural Hawaiian samples are in agreement with the model proposed by *Chemtob and Rossman* (2014).

Surfaces showing silica signatures in the VNIR and MIR provide the best candidates for potential fumarolic deposits. For example, hydrated silica has been identified in several locations through VNIR detections from the Compact Reconnaissance Imaging Spectrometer for Mars (CRISM) at Western Hellas (*Bandfield,* 2008), plains near Melas Chasma and Juventae Chasma (*Milliken et al.,* 2008), Isidis Basin (*Ehlmann et al.,* 2009), Northern Syrtis Major (*Ehlmann et al.,* 2009; *Smith and Bandfield,* 2012), Toro Crater (*Marzo et al.,* 2010), Nili Patera (e.g. *Skok et al.,* 2010), Terra Sirenum (*Wray et al.,* 2011), and Noctis Labyrinthus (*Weitz et al.,* 2011). Hydrated silica has also been identified in MIR data from the Thermal Emission Spectrometer (TES) and Thermal Emission Imaging System (THEMIS) at Western Hellas Basin (*Bandfield,* 2008) and along the dichotomy boundary (*Bandfield and Amador,* 2016). Hydrothermal processes have been inferred for most of these regions; however, it is difficult to rule out other origins from orbital data alone. Nevertheless, this work provides strong support for those interpretations.

5. Implications:

This work provides a unique infrared spectral library that includes Martian analog materials that were altered in an active terrestrial solfatara (hydrothermal) setting. Hydrothermal environments are of particular interest as they potentially indicate habitable conditions. Among the techniques to detect potential hydrothermal/habitable conditions on Mars, visible and infrared spectroscopic remote sensing provides the greatest coverage at the highest spatial resolution,

allowing for assessment of spatial and/or temporal variability in surface conditions. Key constraints on the habitability and astrobiological potential of ancient aqueous environments are provided through detection and interpretation of secondary mineral assemblages; thus, spectral detection of fumarolic alteration assemblages observed from this study on Mars would suggest a region that could have hosted a habitable environment. Alteration assemblages that were potentially derived from hydrothermal systems have been detected *in situ* on Mars at Gusev Crater and Meridiani Planum. *Kraft et al.* (2003) suggest that secondary amorphous silica may account for the spectral signatures observed for ST2, exhibiting the potential widespread nature of this type of alteration. Using the spectral library provided here, the search for hydrothermal systems on Mars can be extended to other locations using orbital measurements of reflectance and emission spectra, which are sensitive to mineral species and abundance.

6. Acknowledgements

All field work reported here that was conducted within Hawai‘i Volcanoes National Park (HVNP) was conducted under National Park Service (NPS) Scientific Research and Collection Permit # HAVO-2012-SCI-0025 as part of NPS Study # HAVO-00420. This work was supported by the RIS4E node of NASA's Solar System Exploration Virtual Institute. A. D. R. also acknowledges support from the Mars Fundamental Research Program NNX13AG82G. The authors would like to thank Steve Ruff for contributing silica reference spectra. NSF-EAR 0923224 awarded to Franklin and Marshall College facilitated a substantial upgrade of both XRD and XRF instrumentation. We also would like to thank Joseph Michalski and Rebecca Greenberger for their insightful reviews. Lastly, Mertzman thanks Karen R. Mertzman for her ongoing meticulous work in the X-ray lab without which there would be much less high quality data in the world.

References:

Anderson, J.H. and K.A. Wickersham (1964), Near infrared Characterization of Water and Hydroxyl Groups on Silica Surfaces, Surface Science, 2 251-260.

Arvidson, R. E., S.W. Squryes, J.F. Bell III, J.G. Catalano, B.C. Clark, L.S. Crumpler, P. A. de Souza Jr., A. G. Fairén, W. H. Farrand, V. K. Fox, R. Gellert, A. Ghosh, M. P. Golombek, J. P. Grotzinger, E. A. Guinness, K. E. Herkenhoff, B. L. Jolliff, A. H. Knoll, R. Li, S. M. McLennan, D. W. Ming, D. W. Mittlefehldt, J. M. Moore, R. V. Morris, S. L. Murchie, T. J. Parker, G. Paulsen, J. W. Rice, S. W. Ruff, M. D. Smith, and M. J. Wolff (2014), Ancient aqueous environments at Endeavour Crater, Mars, *Science*, 343(6169), 1248097, doi:10.1126/science.1248097.

Baldridge, A. M. (2008), Thermal Infrared Spectral Studies of Sulfates and Chlorides; Applications to Salts on the Martian Surface, Ph.D. Dissertation thesis, 204 pp., Arizona State University, Tempe, AZ.

Baldridge, A.M., P.R. Christensen (2009), Laboratory Technique for Thermal Emission Measurement of Hydrated Minerals: Applied Spectroscopy, v. 63, p. 678-688.

Bandfield, J.L. (2008), High-silica deposits of an aqueous origin in western Hellas Basin, Mars. Geophysical Research Letters, 35, 142–147. http://dx.doi.org/10.1029/ 2008GL033807.

Bandfield, J. L. and E. S. Amador (2016), Extensive aqueous deposits at the base of the dichotomy boundary in Nilosyrtis Mensae, Mars, Icarus, 275, 29–44.

Bell, J III (2008), The Martian Surface—Composition, Mineralogy, and Physical Properties. New York: Cambridge University Press.

Bigham, J. M., and D. K. Nordstrom (2000), Iron and aluminum hydroxysulfates from acid sulfate waters, in Sulfate Minerals: Crystallography, Geochemistry and Environmental

599 Significance, edited by C. N. Alpers, J. L. Jambor, and D. K. Nordstrom, pp. 351 – 403,
600 Mineral. Soc. Of Am., Washington, D. C.
601 Bishop, J. L., and E. Murad (1996), Schwertmannite on Mars? Spectroscopic analyses of
602 schwertmannite, its relationship to other ferric minerals, and its possible presence in the
603 surface material on Mars, in *Mineral Spectroscopy: A Tribute to Roger G. Burns*, edited
604 by M. D. Dyar et al., Spec. Publ. Geochem. Soc., 5, 337–358.
605 Bishop, J.L., Schiffman P., Lane M.D., and Dyar M.D. (2005a) Solfataric alteration in Hawaii as
606 a mechanism for formation of the sulfates observed on Mars by OMEGA and the MER
607 instruments. Lunar and Planetary Science Conference, XXVI, LPI, Houston,
608 Abstract #1456.
609 Bishop, J.L., Dyar M.D., Lane M.D., and Bandfield J.F. (2005b), Spectral identification of
610 hydrated sulfates on Mars and comparison with acidic environments on Earth.
611 International Journal of Astrobiology, 3, 275-285.Bishop, J.L. , P. Schiffman, E. Murad,
612 M.D. Dyar, A. Drief, M.D.
613 Bishop, J.L., P. Schiffman, E. Murad, M.D. Dyar, A. Drief, M.D. Lane (2007), Characterization
614 of alteration products in tephra from Haleakala, Maui: a visible-infrared spectroscopy,
615 Mössbauer spectroscopy, XRD, EMPA and TEM study. Clay Miner., 55 (1), pp. 1-17.
616 Bishop, J.L., E.Z.Noe Dobrea, N.K. McKeown, M. Parente, B.L. Ehlmann, J.R. Michalski, R.E.
617 Milliken, F. Poulet, G.A. Swayze, J.F. Mustard, S.L. Murchie, and J.-.,P. Bibring (2008)
618 Phyllosilicate diversity and past aqueous activity revealed at Mawrth Vallis, Mars.
619 Science, 321, 830-833. Bishop, J.L., Lane M.D., Dyar M.D., King S.J., Brown A.J., and
620 Swayze G. (2014), Spectral properties of Ca-sulfates: Gypsum, bassanite and anhydrite.
621 American Mineralogist, 99, 2105-2115.

622 Bishop, J. L., E. Murad, and M. D. Dyar (2015), Akaganéite and schwertmannite: Spectral
623 properties and geochemical implications of their possible presence on Mars, American
624 Mineralogist, 100(4), 738–746.
625 Burns R.D., D.S. Fisher (1990), Iron–sulfur mineralogy of Mars: magmatic evolution and
626 chemical weathering products, J. Geophys. Res., 95 pp., 14415–14421.
627 Chemtob, S.M, G,R. Rossman (2014), Timescales and mechanisms of formation of amorphous
628 silica coatings on fresh basalts at Kīlauea Volcano, Hawai'i, Journal of Volcanology and
629 Geothermal Research, Volume 286, 1 October 2014, Pages 41-54, ISSN 0377-0273.
630 Chemtob, S.M., Jolliff, B.L., Rossman, G.R., Eiler, J.M., Arvidson, R.E., (2010), Silica coatings
631 in the Ka'u Desert, Hawaii, a Mars analog terrain: a micromorphological, spectral,
632 chemical, and isotopic study. Journal of Geophysical Research, 115, E04001.
633 Christensen, P.R., J. L. Bandfield, R. N. Clark, K. S. Edgett, V. E. Hamilton, T. Hoefen, H. H.
634 Kieffer, R. O. Kuzmin, M. D. Lane, M. C. Malin, R. V. Morris, J. C. Pearl, R. Pearson, T.
635 L. Roush, S. W. Ruff, and M. D. Smith (2000), Detection of crystalline hematite
636 mineralization on Mars by the Thermal Emission Spectrometer: Evidence for near-
637 surface water. Journal of Geophysical Research, 105:9623–9642.
638 Clark, B. C. (1993), Geochemical components in Martian soil. Geochimica et Cosmochimica
639 Acta ,57, 4575–4581.
640 Clark, B.C., R.V. Morris, S.M. McLennan, R. Gellert, B. Jolliff, A.H. Knoll, S.W. Squyres, T.K.
641 Lowenstein, D.W. Ming, N.J. Tosca, A. Yen, P.R. Christensen, S.P. Gorevan, J.
642 Brückner, W.M. Calvin, G. Dreibus, W.H. Farrand, G. Klingelhöfer, H. Waenke, J.
643 Zipfel, J.F. Bell III, J.P. Grotzinger, H.Y. McSween Jr., and R. Rieder (2005), Chemistry

644 and mineralogy of outcrops at Meridiani Planum, Earth and Planetary Science Letters.
645 240, 73-94.
646 Clark, R. N. and T. L. Roush (1984), Reflectance spectroscopy: Quantitative analysis techniques
647 for remote sensing applications, Journal of Geophysical Research, 89(B7), 6329–6340,
648 doi:10.1029/JB089iB07p06329.
649 Cloutis, E.A., F.C. Hawthorne, S.A. Mertzman, Krenn, K., M.A. Craig, D. Marcino, M. Methot,
650 J. Strong, J.F. Mustard, D.L. Blaney, J.F. Bell III, and F. Vilas (2006), Detection and
651 discrimination of sulfate minerals using reflectance spectroscopy. Icarus 184, 121-157.
652 doi:10.1016/j.icarus.2006.04.003
653 Costello E.K., S.R.P. Halloy, S.C. Reed, P. Sowell, and S.K. Schmidt (2009), Fumarole-
654 supported islands of biodiversity within a hyperarid, high-elevation landscape on
655 Socompa Volcano, Puna de Atacama, Andes. Applied Environmental
656 Microbiology, 2009; 75:735–747.
657 Crisp, J., A.B. Kahle, and E.A. Abbott (1990), Thermal infrared spectral character of Hawaiian
658 basaltic glasses. Journal of Geophysical Research, 95, 21657 – 21669.
659 Dorn, R.I. (2012), Formation of silica glaze rock coatings through water vapor interactions.
660 Physical Geography, 33 (1), 21–31.
661 Eastes, J.W. (1989), Spectral properties of halite-rich mineral mixtures: Implications for middle
662 infrared remote sensing of highly saline environments, Remote Sensing of Environment,
663 27:289-304.
664 Ehlmann, B. L., J.F. Mustard, G.A. Swayze, R.N. Clark, J.L. Bishop, F. Poulet, D.J. Des Marais,
665 L.H. Roach, R.E. Milliken, J.J. Wray, O. Barnouin-Jha, and S.L. Murchie (2009),
666 Identification of hydrated silicate minerals on Mars using MRO-CRISM: Geologic context

667 near Nili Fossae and implications for aqueous alteration, Journal of Geophysical Research,
668 114, E00D08, doi:10.1029/2009JE003339.
669 Ellis D.G., R.W. Bizzoco, and S.T. Kelley (2008), Halophilic Archaea determined from
670 geothermal steam vent aerosols. Environmental Microbiology, 10:1582–1590.
671 El-Shamy, T. M., J. Lewins, and R. W. Douglas (1972), The dependence of the pH on the
672 decomposition of glasses by aqueous solutions, Journal of the Society of Glass
673 Technology, 13(3), 81 – 87.
674 Glotch, T.D., R.V. Morris, P.R. Christensen, and T.G. Sharp (2004), Effect of precursor
675 mineralogy on the thermal infrared emission spectra of hematite: application to Martian
676 hematite mineralization. Journal of Geophysical Research, 109.
677 Glotch, T. D., and M. D. Kraft (2008), Thermal transformations of akaganéite and lepidocrocite
678 to hematite: Assessment of possible precursors to Martian crystalline hematite, Physics
679 and Chemistry of Minerals, 35, 569-581.
680 Golden D.C., R.V. Morris, D.W. Ming, H.V. Lauer Jr., and S.R. Yang (1993), Mineralogy of
681 three slightly palagonitized basaltic tephra samples from the summit of Mauna Kea,
682 Hawaii. JGR 98, 3401-3411.
683 Golden, D. C., D. W. Ming, R. V. Morris, and S. A. Mertzman (2005), Laboratory-simulated
684 acid-sulfate weathering of basaltic materials: Implications for formation of sulfates at
685 Meridiani Planum and Gusev crater, Mars, J. Geophys. Res., 110, E12S07.
686 Goryniuk, M.C., B.A. Rivard, and B. Jones (2004), The reflectance spectra of opal-A (0.5-25
687 μm) from the Taupo Volcanic Zone: Spectra that may identify hydrothermal systems on
688 planetary surfaces. Geophys. Res. Lett. 31, n/a-n/a. doi:10.1029/2004GL021481

689 Halloy S. (1991), Islands of life at 6000 m altitude—the environment of the highest autotrophic
690 communities on Earth (Socompa Volcano, Andes) Arctic and Alpine Research.;23:247–
691 262.
692 Hamilton, V. E., R. V. Morris, J. E. Gruener, and S. A. Mertzman (2008), Visible, near-infrared,
693 and middle infrared spectroscopy of altered basaltic tephras: Spectral signatures of
694 phyllosilicates, sulfates, and other aqueous alteration products with application to the
695 mineralogy of the Columbia Hills of Gusev Crater, Mars: Journal of Geophysical
696 Research-Planets, v. 113, p. E12S43.
697 Haskin L.A., A. Wang, B.L. Jolliff, H.Y. McSween, B.C. Clark, D.J. Des Marais, S.M.
698 McLennan, N.J. Tosca, J.A. Hurowitz, J.D. Farmer, A. Yen A, S.W. Squyres, R.E.
699 Arvidson, G. Klingelhöfer, C. Schröder, P.A. de Souza Jr., D.W. Ming, R. Gellert, J.
700 Zipfel, J. Brückner, J.F. Bell III, K. Herkenhoff, P.R. Christensen, S. Ruff, D.L. Blaney,
701 S. Gorevan, N.A. Cabrol, L. Crumpler, J. Grant, and L. Soderblom (2005), Water
702 alteration of rocks and soils on Mars at the Spirit rover site in Gusev crater. Nature, 436,
703 66-69.
704 Hunt, G. R., and L. M. Logan (1972), Variation of Single Particle Mid-Infrared Emission
705 Spectrum with Particle Size, Appl. Opt. 11, 142-147.
706 Hunt, G. R., and R. K. Vincent (1968), The behavior of spectral features in the infrared emission
707 from particulate surfaces of various grain sizes, Journal of Geophysical.
708 Research, 73(18), 6039–6046, doi:10.1029/JB073i018p06039.
709 Hurowitz, J. A., and W. W. Fischer (2014), Contrasting styles of water–rock interaction 862 at
710 the Mars Exploration Rover landing sites, Geochimica et Cosmochimica Acta, 127, 863
711 25-38.

712 Hurowitz, J. A., S. M. McLennan, N. J. Tosca, R. E. Arvidson, J. R. Michalski, D. W. Ming, C.
713 Schröder, and S. W. Squyres (2006), In situ and experimental evidence for acidic
714 weathering of rocks and soils on Mars, Journal of Geophysical Research, 111, E02S19.
715 Hurowitz, J.A., and S.M. McLennan (2007), A ~ 3.5 Ga record of water-limited, acidic
716 weathering conditions on Mars, Earth and Planetary Science Letters, Volume 260, Issues
717 3–4, 30 August 2007, Pages 432-443, ISSN 0012-821X.
718 Kraft M.D., J.R. Michalski, and T.G. Sharp (2003), Effects of pure silica coatings on thermal
719 emission spectra of basaltic rocks: Considerations for Martian surface mineralogy, GRL
720 30, 2288.
721 Lane, M.D. (2007), Mid-infrared emission spectroscopy of sulfate and sulfate-bearing minerals.
722 American Mineralogist, 92, pp. 1–18.
723 Lane, M.D., J.L. Bishop, M.D. Dyar, T.H. Hiroi, S.A. Mertzman, D.L. Bish, P.L. King, and A.D.
724 Rogers (2015), Mid-infrared emission spectroscopy and visible/near-infrared reflectance
725 spectroscopy of Fe-sulfate minerals. American Mineralogist, 100, pp. 66-82.
726 Lichtenberg, K. A., R.E. Arvidson, R.V. Morris, S.L. Murchie, J.L. Bishop, D.F. Remolar, T.D.
727 Glotch, E.N. Dobrea, J.F. Mustard, J. Andrews-Hanna, and L.H. Roach
728 (2010), Stratigraphy of hydrated sulfates in the sedimentary deposits of Aram Chaos,
729 Mars, Journal of Geophysical Research, 115, E00D17.
730 Madden M. E., R. J. Bodnar, and J. D. Rimstidt (2004), Jarosite as an indicator of water-limited
731 chemical weathering on Mars. Nature 431, 821–823.
732 Marzo, G.A., A. F. Davila, L. L. Tornabene, J. M. Dohm, A. G. Fairén, C. Gross, T. Kneissl, J.
733 L. Bishop, T. L. Roush, and C. P. McKay (2010), Evidence for Hesperian impact-induced
734 hydrothermalism on Mars. Icarus, 208, 667–683.

735 McAdam, A. C., M. Y. Zolotov, M. V. Mironenko, and T. G. Sharp (2008), Formation of silica
736 by low-temperature acid alteration of Martian rocks: Physical-chemical
737 constraints, Journal of Geophysical Research, 113, E08003, doi:10.1029/2007JE003056.
738 McCanta, M.C., M.D. Dyar, and A.H. Treiman (2014), Alteration of Hawaiian basalts under
739 sulfur-rich conditions: Applications to understanding surface–atmosphere interactions on
740 Mars and Venus. American Mineralogist, 99, pp. 291–302.
741 McCollom, T. M., and B. M. Hynek (2005), A volcanic environment for bedrock diagenesis at
742 Meridiani Planum, Mars, Nature, 438, 1129-1131.
743 McKeown, N.K., J.L. Bishop, J. Cuadros, S. Hillier, E. Amador, H.D. Makarewicz, M. Parente,
744 and E.A. Silver (2011), Interpretation of reflectance spectra of clay mineral-silica
745 mixtures; implications for Martian clay mineralogy at Mawrth Vallis, Clays and Clay
746 Minerals, v. 59, p. 400-415, doi: 10.1346/CCMN.2011.0590404.
747 McLennan, S. M. (2003), Sedimentary silica on Mars, Geology, 31(4), 315 – 318,
748 doi:10.1130/0091-7613(2003)0312.0.CO;2.
749 Milliken, R.E., G.A. Swayze, R.E. Arvidson, J.L. Bishop, R.N. Clark, B.L. Ehlmann, R.O.
750 Green, J.P. Grotzinger, R.V. Morris, S.L. Murchie, J.F. Mustard, and C. Weitz (2008),
751 Opaline silica in young deposits on Mars. Geology, 36, 847– 850.
752 http://dx.doi.org/10.1130/G24967A.1.
753 Ming D. W., D. W. Mittlefehldt, R. V. Morris, D. C. Golden, R. Gellert, A. Yen, B.C. Clark, S.
754 W. Squyres, W. H. Farrand, S. W. Ruff, R. E. Arvidson, G. Klingelhöfer, H. Y.
755 McSween, D. S. Rodionov, C. Schröder, P. A. de Souza, and A. Wang (2006),
756 Geochemical and mineralogical indicators for aqueous processes in the Columbia Hills of
757 Gusev crater, Mars. Journal of Geophysical Research, 111, E02S12.

Minitti, M. E., C. M. Weitz, M. D. Lane, and J. L. Bishop (2007), Morphology, chemistry, and spectral properties of Hawaiian rock coatings and implications for Mars, Journal of Geophysical Research, 112, E05015, doi:10.1029/2006JE002839.

Morris, R. V., H. V. Lauer Jr., C. A. Lawson, E. K. Gibson Jr., G. A. Nace, and C. Stewart (1985), Spectral and other physicochemical properties of submicron powders of hematite (α-Fe_2O_3), maghemite (γ-Fe_2O_3), magnetite (Fe_3O_4), goethite (α-FeOOH), and lepidocrocite (γ-FeOOH), *J. Geophys. Res.*, 90, 3126–3144.

Morris, R. V., G. Klingelhöfer, C. Schröder, D. S. Rodionov, A. Yen, D. W. Ming, P. A. de Souza Jr., I. Fleischer, T. Wdowiak, R. Gellert, B. Bernhardt, E. N. Evlanov, B. Zubkov, J. Foh, U. Bonnes, E. Kankeleit, P. Gütlich, F. Renz, S. W. Squyres, and R. E. Arvidson (2006), Mössbauer mineralogy of rock, soil, and dust at Gusev crater, Mars: Spirit's journey through weakly altered olivine basalt on the plains and pervasively altered basalt in the Columbia Hills, Journal of Geophysical Research, 111, E02S13.

Morris, R. V., D.C. Golden, J.F. Bell III, T.D. Shelfer, A.C. Scheinost, N.W. Hinman, G. Furniss, S.A. Mertzman, J.L. Bishop, D.W. Ming, C.C. Allen, D.T. Britt (2000a), Mineralogy, composition and alteration of Mars Pathfinder rocks and soils: Evidence from multispectral, elemental and magnetic data on terrestrial analogue, SNC meteorite and Pathfinder samples, Journal of Geophysical Research, 105, 1757– 1817.

Morris, R.V., T. Graff, M.D. Lane, D.C. Golden, C.S. Schwandt, D.W. Ming, T.D. Shelfer, S.A. Mertzman, J. F. Bell, J. Crisp, and P.R. Christensen (2000b), Acid sulfate alteration products of a tholeiitic basalt: Implications for interpretation of Martian thermal emission spectra, Lunar and Planetary Science Conference, XXXI, Abs. 2014.

780 Morris, R.V., D.W. Ming, T.G. Graff, R.E. Arvidson, J.F. Bell, S.W. Squyres, S.A. Mertzman,
781 J.E. Gruener, D.C. Golden, L. Le, G.A. Robinson (2005), Hematite spherules in basaltic
782 tephra altered under aqueous, acid-sulfate conditions on Mauna Kea volcano, Hawaii:
783 Possible clues for the occurrence of hematite-rich spherules in the Burns formation at
784 Meridiani Planum, Mars, Earth and Planetary Science Letters, 240, 168-178.
785 Morris, R.V., D. W. Ming, R. Gellert, A. Yen, B. C. Clark, T. G. Graff, R. E. Arvidson, S. W.
786 Squyres, and the Athena and CRISM Science Teams (2008), The hydrothermal system at
787 Home Plate in Gusev crater, Mars: Formation of high silica material by acid-sulfate
788 alteration of basalt. Lunar and Planetary Science Conference, XXIX, Abs. 2208.
789 Morris, R.V., E.B. Rampe, T.G. Graff, P.D. Archer, Jr., L. Le, D.W. Ming, and B. Sutter
790 (2015) Transmission X-ray diffraction (XRD) patterns relevant to the MSL CheMin amorphous
791 component: sulfates and silicates. Lunar and Planetary Science Conference, XXVI, Abs.
792 #2434.
793 Mustard, J. F., and J. E. Hayes (1997), Effects of hyperfine particles on reflectance spectra from
794 0.3 to 25 μm, Icarus, 125, 145–163.
795 Niles P. B., and J. Michalski (2009), Meridiani Planum sediments on Mars formed through
796 weathering in massive ice deposits. Nat. Geosci. 2, 215–220.
797 Ramsey, M.S., and P.R. Christensen (1998), Mineral abundance determination: Quantitative
798 deconvolution of thermal emission spectra. Journal of Geophysical Research, 103 (B1),
799 577–597.
800 Rice, M. S., E. A. Cloutis, J. F. Bell III, D. L. Bish, B. H. Horgan, S. A. Mertzman, M. A. Craig,
801 R. W. Renaut, B. Gautason, and B. Mountain (2013), Reflectance spectra diversity of

802 silica-rich materials: Sensitivity to environment and implications for detections on Mars,
803 Icarus, 223(1), 499–533, doi:10.1016/j.icarus.2012.09.021.
804 Rogers, A.D., and Aharonson, O. (2008), Mineralogical composition of sands in Meridiani
805 Planum determined from MER data and comparison to orbital measurements. Journal of
806 Geophysical Research – Planets, 113, E06S14.
807 Ruff, S. W., J.D. Farmer, W.M. Calvin, K.E. Herkenhoff, J.R. Johnson, R.V. Morris, M.S. Rice,
808 R.E. Arvidson, J.F. Bell III, P.R. Christensen, and S.W. Squyres (2011), Characteristics,
809 distribution, origin, and significance of opaline silica observed by the Spirit rover in
810 Gusev crater, Mars, J. Geophys. Res., 116, E00F23.
811 Salisbury, J. W., and A. Wald (1992), The role of volume scattering in reducing spectral contrast
812 of Restrahlen bands in spectra of powdered minerals, Icarus, 96, 121-128.
813 Schiffman, P., Spero, H.J., Southard, R.J., and Swanson, D.A. (2000), Controls on
814 palagonitization versus pedogenic weathering of basaltic tephra: Evidence from the
815 consolidation and geochemistry of the Keanakako'i Ash Member, Kilauea Volcano.
816 Geochemistry, Geophysics, Geosystems, 1, 1040.
817 Schiffman, P., Zierenberg, R., Marks, N., Bishop, J.L., and Dyar, M.D. (2006), Acid-fog
818 deposition at Kilauea volcano: A possible mechanism for the formation of siliceous-
819 sulfate rock coatings on Mars. Geology 34, 921-924.
820 Schmidt, M.E., S.W. Ruff, T.J. McCoy, W. H. Farrand, J. R. Johnson, Ralf Gellert, D. W.
821 Ming, R.V. Morris, N. Cabrol, K.W. Lewis, and C. Schroeder (2008), Hydrothermal
822 origin of halogens at Home Plate, Gusev Crater. Journal of Geophysical Research, 113,
823 E06S12.

824 Seelos, K. D., R. E. Arvidson, B. L. Jolliff, S. M. Chemtob, R. V. Morris, D. W. Ming, and G. A.
825 Swayze (2010), Silica in a Mars analog environment: Ka'u Desert, Kilauea Volcano,
826 Hawaii, Journal of Geophysical Research ,115, E00D15, doi:10.1029/2009JE003347.
827 Sklute, E. (2015), On the Subject of Analyzing Iron and Sulfur Bearing Minerals from Three
828 Extreme Environments: Geological Carbon Sequestration, Acid Mine Drainage, and
829 Mars. Ph.D. Dissertation thesis, 433 pp., Stony Brook University, Stony Brook, NY.
830 Skok, J. R., J. F. Mustard, B. L. Ehlmann, R. E. Milliken, and S. L. Murchie (2010), Silica
831 deposits in the Nili Patera caldera on the Syrtis Major volcanic complex on Mars, Nature
832 Geoscience, **3**(12), 838–841.
833 Smith, M. R., and J. L. Bandfield (2012), Geology of quartz and hydrated silica-bearing deposits
834 near Antoniadi Crater, Mars, J. Geophys. Res., **117**, E06007, doi:10.1029/2011JE004038
835 Squyres, S., McCoy, A.S. McEwen, H.Y. McSween, D.W. Ming, J M. Moore, R.V. Morris, T.J.
836 Parker, J.W. Rice Jr., S. Ruff, M. Schmidt, C. Schröder, L.A. Soderblom, and A. Yen
837 (2007), Pyroclastic activity at Home Plate in Gusev Crater, Mars. Science, 316, 738-742.
838 Squyres, S. W., R.E. Arvidson, J.F. Bell III, F. Calef III, B.C. Clark, B.A. Cohen, L.A.
839 Crumpler, P.A. de Souza Jr., W.H. Farrand, R. Gellert, J. Grant, K.E. Herkenhoff, J.A.
840 Hurowitz, J.R. Johnson, B.L. Jolliff, A.H. Knoll, R. Li, S.M. McLennan, D.W.
841 Ming, D.W. Mittlefehldt, T.J. Parker, G. Paulsen, M.S. Rice, S.W. Ruff, C.
842 Schröder, A.S. Yen, K. Zacny (2012), Ancient impact and aqueous processes and
843 Endeavour Crater, Mars, *Science*, 336, 570–576, doi:10.1126/science.1220476.
844 Tosca, N.J., S.M. McLennan, D.H. Lindsley, and M.A.A. Schoonen (2004), Acid-sulfate
845 weathering of synthetic Martian basalt: The acid fog model revisited, Journal of Geophysical
846 Research, 109, E05003.

Wald, A. E., and J. W. Salisbury (1995) The thermal infrared directional emissivity of quartz, Journal of Geophysical Research, 100, 24,665-24,675.

Weitz, C.M., Bishop, J.L., Thollot, P., Mangold, N., and Roach, L.H. (2011), Diverse mineralogies in two troughs of Noctis Labyrinthus. Geology 39, 899–902, doi: 10.1130/G32045.1.

Wray, J.J., R.E. Milliken, C.M. Dundas, G.A. Swayze, J.C. Andrews-Hanna, A.M. Baldridge, M.Chojnacki, J.L. Bishop, B.L. Ehlmann, S.L. Murchie, R.N. Clark, F.P. Seelos, L.L. Tornabene, and S.W. Squyres (2011), Columbus crater and other possible groundwater-fed paleolakes of Terra Sirenum, Mars. Journal of Geophysical Research, 116, E01001, doi: 10.1029/2010JE003694.

Wyatt, M. B., V. E. Hamilton, H. Y. McSween Jr., P. R. Christensen, and L. A. Taylor (2001), Analysis of terrestrial and Martian volcanic compositions using thermal emission spectroscopy: 1. Determination of mineralogy, chemistry, and classification strategies, Journal of Geophysical Research, 106(E7), 14711–14732.

Yant, M., A. D. Rogers, H. Nekvasil, Y.-Y. S. Zhao, and T. Bristow (2016), Spectral characterization of acid weathering products on Martian basaltic glass, Journal of Geophysical Research - Planets, 121, doi:10.1002/2015JE004969.

Yen, A. S., R.V. Morris, B.C. Clark, R. Gellert, A.T. Knudson, S. Squyres, D.W. Mittlefehldt, D.W. Ming, R. Arvidson, T. McCoy, M. Schmidt, J. Hurowitz, R. Li, and J.R. Johnson (2008), Hydrothermal processes at Gusev Crater: An evaluation of Paso Robles class soils, J. Geophys. Res. Journal of Geophysical Research, 113, E06S10, doi:10.1029/2007JE002978.

869 Young, K. E., C. A. Evans, and K. V. Hodges (2011), Laboratory Tests of a Handheld X-Ray
870 Fluorescence Spectrometer: A Tool for Planetary Exploration, American Geophysical
871 Union, Fall Meeting, Abstract P43B-1672.
872 Young, K. E., C. A. Evans, and K. V. Hodges (2012), Evaluating Handheld X-Ray Fluorescence
873 (XRF) Technology in Planetary Exploration: Demonstrating Instrument Stability and
874 Understanding Analytical Constraints and Limits for Basaltic Rocks, Lunar and Planetary
875 Science Conference, XLIII, Abstract 2628.
876 Young, K. E., J. E. Bleacher, C. A. Evans, A. D. Rogers, G. Ito, Z. Arzoumanian, and K.
877 Gendreau (2015), Examining Volcanic Terrains Using In Situ Geochemical
878 Technologies: Implications for Planetary Field Geology, Lunar and Planetary Science
879 Conference, XLVI, Abstract 1658.
880 Young, K. E., Evans, C. A., Hodges, K. V., Bleacher, J. E., & Graff, T. G. (2016). A review of
881 the handheld X-ray fluorescence spectrometer as a tool for field geologic investigations
882 on Earth and in planetary surface exploration. *Applied Geochemistry*, *72*, 77-87.
883 DOI: 10.1016/j.apgeochem.2016.07.003

884 **Figure Captions:**

885 **Figure 1: a**) Image of the volcanic vent from which the samples were collected, **b-i)** close-up
886 images of the samples in situ, **j-p)** laboratory images of the HI_15_MHY samples, and **q-w)**
887 laboratory images of the HI_15_Solf samples. See text for a description of the sample labels.

888 **Figure 2:** Thermal emission signatures of the collected samples grouped based on similarities of
889 dominant spectral features into **a)** Group 1, silica-dominated, **b)** Group 2, Ca-sulfate-dominated,
890 **c)** Group 3, Fe-sulfate-dominated, and **d)** Group 4 (silica/Fe-oxide-dominated). The reflectance
891 spectra are separated into groups based on the MIR groups established in panels a-d, **e)** Group 1,

892 **f)** Group 2, **g)** Group 3, and **h)** Group 4. Vertical lines indicate features discussed in text. The
893 spectra have been offset along the y-axis for clarity. Gp = gypsum, Ah = anhydrite, Ak =
894 akaganéite, Ml = melanterite, Al = alunogen, Cq = coquimbite, Hm = hematite. The library
895 spectra used here were not measured in this study and include silica sinter, microporous silica,
896 amorphous silica (*Ruff et al.,* 2011), gypsum (*Lane et al.,* 2007), coquimbite (*Lane et al.,* 2015)
897 alunogen (*Lane unpublished*), and hematite (*Christensen et al.,* 2000) for the MIR. In the VNIR,
898 the library spectra include basaltic glass (*Yant et al.,* 2016), silicic acid, opal-CT (*Rice et al.,*
899 2013), gypsum (RELAB ID: C1JB557), akaganéite (RELAB ID: 397F212D), melanterite
900 (RELAB ID: CASF44), copiapite (RELAB ID: C1JBA51), and anhydrite (RELAB ID:
901 C1JB641A).
902 **Figure 3:** Linear least squares analysis models for the average thermal emission spectrum for
903 each group, **a)** Group 1-1 **b)** Group 1-2, **c)** Group 1-3, **d)** Group 1-4, **e)** Group 2, **f)** Group 3, and
904 **g)** Group 4. The y-axis has been offset for clarity.
905 **Figure 4:** Secondary electron images of HI_15_MHY samples: Group 1-1: **a)**
906 HI_15_MHY_001 exhibiting a Si-rich coating (cross) overlying a Al, Ca, Mg, Fe-rich glass
907 (square), **b)** HI_15_MHY_002a exhibiting a Si-rich surface (cross), and **c)** HI_15_MHY_002b
908 exhibiting a Si-rich coating (cross); Group 1-2: **d)** HI_15_MHY_003 exhibiting Si-rich material
909 (cross) and Ca-sulfate (square) and **e)** HI_15_MHY_005 exhibiting Si-rich surface (cross), Ca-
910 sulfate (square), Fe-Ti-oxide (circle); Group 1-4: **f)** HI_15_MHY_007a exhibiting Si-rich
911 material (cross) and Ca-sulfate (square); Group 2: HI_15_MHY_007b exhibiting **g)** Si-rich clast
912 and **h)** Ca-sulfate rich clast; and Group 3: **i)** HI_15_MHY_006 exhibiting Si-rich material (cross)
913 and Fe-Ti-oxide (square).

914 **Figure 5:** XRD patterns for the three samples that exhibited amorphous humps consistent with
915 more Si-rich material than basaltic glass, **a)** HI_15_MHY_002b, **b)** HI_15_MHY_007b, and **c)**
916 HI_15_Solf_002_2.
917 **Figure 6: a)** Handheld XRF data separated into groups determined using a minimum distance
918 clustering algorithm on chemical data for each sample. Plots of b) Al vs. Si contents and c) Fe
919 vs. Si contents for the natural fumarolic materials. The outlined boxes represent the XRF
920 groupings and the color of the points represent the MIR groupings.
921 **Figure 7**: Comparison of the spectral signatures for the laboratory isochemically altered
922 materials (sulfate-dominated) with the natural fumarolic altered materials (silica-dominated) in
923 both the **a)** MIR and **b)** VNIR wavelength ranges. Red shaded areas correspond to sulfate-related
924 features and blue shaded areas correspond to silica-related features.
925

This is a preprint, the final version is subject to change, of the American Mineralogist (MSA)
Cite as Authors (Year) Title. American Mineralogist, in press.
DOI: http://dx.doi.org/10.2138/am-2018-6238

Table 1. Previous studies of Hawaiian basalt and tephra in situ alteration from a planetary perspective.

	Hawaiian Material	Conditions	Analytical techniques[A]	Secondary phases
Bishop et al., 2005a	Solfataric alteration of ash under 1974 flow in Halemaumau crater	In situ, hydrothermal alteration	VNIR, MIR, SEM, EMP, XRD, MB	Opal-A, gypsum, jarosite, phyllosilicates
***Crisp et al.*, 1990**	Basalt lava flows, Mauna Loa and Kilauea Volcano	In situ, acid alteration	MIR, EMP	Amorphous silica, Fe-Ti-oxides
***Golden et al.*, 1993**	Palagonitized basaltic tephra, Summit of Mauna Kea	In situ, hydrothermal alteration	Diffuse reflectance, FIR, XRD, MB, EMP	Fe-Ti-oxides, erionite, smectite, np-Ox, Ti-hematite
***Morris et al.*, 2000a**	unaltered, palagonitic, and sulfatetic tephra from Mauna Kea Volcano, steam vent material from Kilauea Volcano	In situ, hydrolytic and acid-sulfate alteration	Diffuse reflectance, XRD, MB, XRF	Nanophase-oxides, glass, silica, Fe-sulfate, Al-sulfate, smectite, Fe-oxides
***Morris et al.*, 2000b**	Tholeiitic basalt from Sulfur Bank	In situ, acidic alteration (pH~4-5)	XRD, MIR	Anatase, nanophase silica, Na-Al-sulfate, Ca-sulfate
Schiffman et al., 2000	Keanakako'I Ash, Kilauea Volcano	In situ, acidic (pH<6) to neutral (pH6.5-7.8)	XRD, SEM	Kaolinite, allophane, imogolite, smectite, opal, palagonitized glass
***Schiffman et al.*, 2006**	Siliceous-sulfate basalt coatings, Ka'u Desert	In situ, low pH alteration	XRD, SEM, VNIR, EMP, MB	Amorphous silica, jarosite, hydrated iron oxides
***Bishop et al.*, 2007**	Basaltic tephra, Halekala, Maui	In situ, hydrothermal alteration	XRD, EMP, SEM, TEM, MB, VNIR, TrIR, MIR	Fe-oxides, phyllosilicates, sulfates, amorphous Al-Si-material
***Minitti et al.*, 2007**	Glass-rich basalts	In situ, low pH alteration	EMP, VNIR, MIR	Hydrated silica with minor Fe, Ti, and S-bearing materials, ferric oxides/oxyhydroxides
***Hamilton et al.*, 2008**	Basaltic tephra, Mauna Kea Volcano	In situ, low – neutral-high pH, ambient – high temperature	XRD, VNIR, MIR	Phyllosilicates, Fe-oxides, kaolinite, smectite, cristobalite, palagonite, Na-(Fe,Al)-sulfate
Chemtob et al., 2010	Surface coatings in Ka'u Desert	In situ, low pH alteration	Raman, TrIR, EMP, NanoSIMS, SEM	Altered glass, anatase, rutile, jarosite
***Seelos et al.*, 2010**	Lava, ash, and solfatara deposits, Ka'u Desert	In situ, low pH alteration	VNIR, Raman, EMP	Amorphous silica, sulfur, Fe-oxides
***McCanta et al.*, 2014**	Solfatara deposits, Halemaumau crater	In situ, low pH (<~2) alteration	SEM, MB, XRD	Amorphous silica overlain by sulfates (Ca, Na-Al, Na-Fe)
***Chemtob and Rossman.*, 2014**	Surface coatings on basalts, Kilauea Volcano	In situ, low pH alteration	SEM, EMP, Raman	Amorphous silica, Fe-Ti-oxides

[A]XRD = X-ray diffraction, MB = Mossbauer, XRF= X-ray fluorescence, MIR = mid-infrared, SEM = scanning electron microscopy, VNIR = visible/near-infrared, EMP = electron microprobe, TrIR = transmission infrared, TEM = transmission electron microscopy, FIR = far-infrared, np-Ox – nanophase ferric oxides.

926

Table 2: Overview of alteration material observed for all of the samples analyzed in this study.

Sample	Vent distance	Sample description	MIR	VNIR[A]	SEM[B]	XRD[C]
HI_15_MHY_001	19.5m	Blue surface coating on basalt	Group 1-1 silica-dominated	silica +/- Fe-oxides	Si-Ti-rich coating	Am
HI_15_MHY_002a	18.0m	White alteration coating on basalt	Group 1-1 silica-dominated	silica, $Fe^{+2/+3}$-sulfate	Si-Fe-Ti-rich coating, Fe-, Ca-sulfates	Am
HI_15_MHY_002b	18.0m	Yellow alteration coating on basalt	Group 1-1 silica-dominated	silica, $Fe^{+2/+3}$-sulfate	Si-rich coating	Am, xtl silica
HI_15_Solf_001_1	n/a	Brown basalt	Group 1-1 silica-dominated	silica, Fe-oxides +/- $Fe^{+2/+3}$-sulfate	n/a	Am
HI_15_Solf_002_1	n/a	Reddish soil	Group 1-1 silica-dominated	silica, Fe-oxides +/- $Fe^{+2/+3}$-sulfate	n/a	Am
HI_15_MHY_003	11.5m	White alteration coating on basalt	Group 1-2 silica-dominated	silica, Fe-oxides	Si-rich coating, Ca-sulfate	Am, Blix
HI_15_MHY_005	4.7m	White encrusted coating on soft red material	Group 1-2 silica-dominated	silica, Fe-oxides	Fe-Ti-oxides, Ca-sulfate, Si-rich coating	Am, Fe-ox
HI_15_Solf_003_2	n/a	White coating on basalt	Group 1-2 silica-dominated	silica, Fe-oxides	n/a	Am
HI_15_Solf_003_3	n/a	Reddish soil	Group 1-2 silica-dominated	silica, Fe-oxides	n/a	Am, Fe-ox, Zeo, K-sulfate
HI_15_Solf_001_2	n/a	White encrusted material on soft red material	Group 1-3 silica-dominated	silica	n/a	Am, Fe-ox
HI_15_Solf_002_3	n/a	White globular crust	Group 1-3 silica-dominated	silica	n/a	Am
HI_15_MHY_007a	4.5m	Yellow/white coating on soft red material	Group 1-4 silica-dominated	silica, Ca-sulfate	Si-rich coating, Ca-sulfate	Am
HI_15_MHY_007b	4.5m	Mm-sized yellow and white grains	Group 2 Ca-sulfate-dominated	silica, Ca-sulfate	Si-rich coating, Ca-sulfate	Am, Ca-sulfate, sulfur
HI_15_Solf_002_2	n/a	White and yellow coating filling topographic lows	Group 3 Fe/Al-sulfate-dominated	silica, Ca-sulfate	n/a	Am
HI_15_MHY_006	4.0m	Yellow/ white encrusted coating on soft red material	Group 4 silica-Fe-oxide-dominated	silica, Fe-oxides +/- $Fe^{+2/+3}$-sulfate	Fe-Ti-oxides, Si-rich coating	Am, xtl silica

[A]Silica indicates opal-CT and/or silicic acid ($SiO_2 \cdot nH_2O$)
[B]SEM analysis was only performed on the HI_15_MHY samples.
[C]Amorphous material could indicate glass, silica, or other amorphous materials which result in a characteristic hump in the XRD pattern.
Xtl silica indicates a crystalline silica phase that produced distinct peaks in the XRD pattern. Am = amorphous material, Blix = blixite, Fe-ox = Fe-oxides, Zeo = zeolite. Fe-oxides could be primary or secondary material.

This is a preprint, the final version is subject to change, of the American Mineralogist (MSA)
Cite as Authors (Year) Title. American Mineralogist, in press.
DOI: http://dx.doi.org/10.2138/am-2018-6238

Figure 1

This is a preprint, the final version is subject to change, of the American Mineralogist (MSA)
Cite as Authors (Year) Title. American Mineralogist, in press.
DOI: http://dx.doi.org/10.2138/am-2018-6238

Figure 2

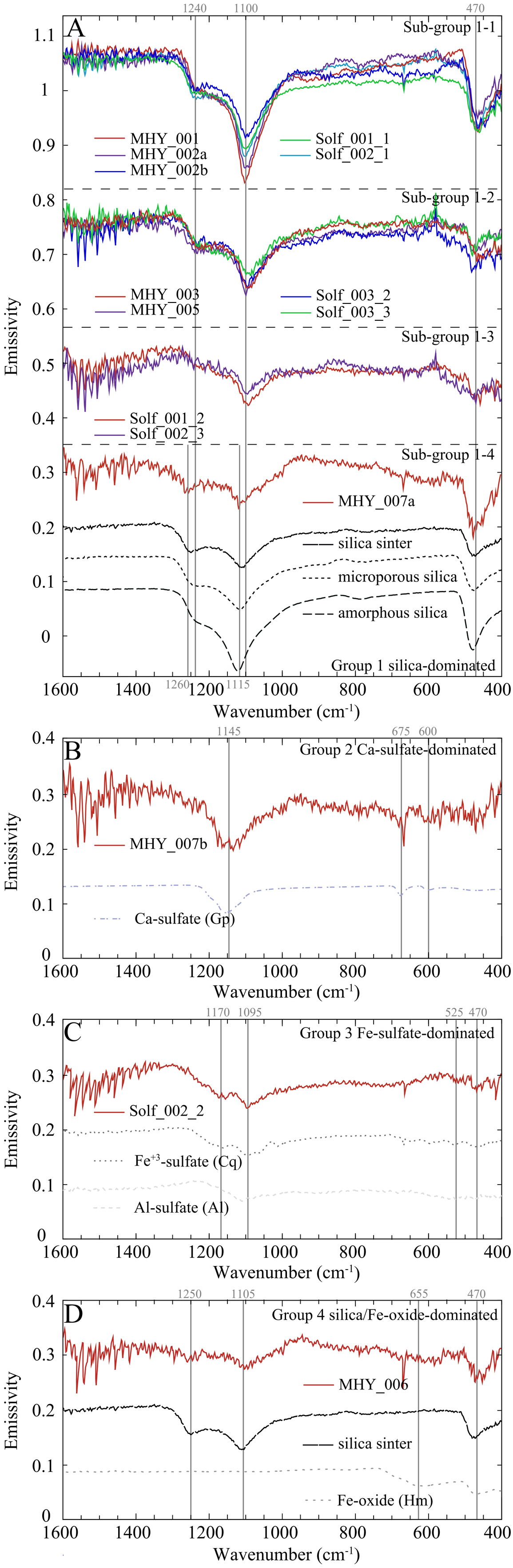

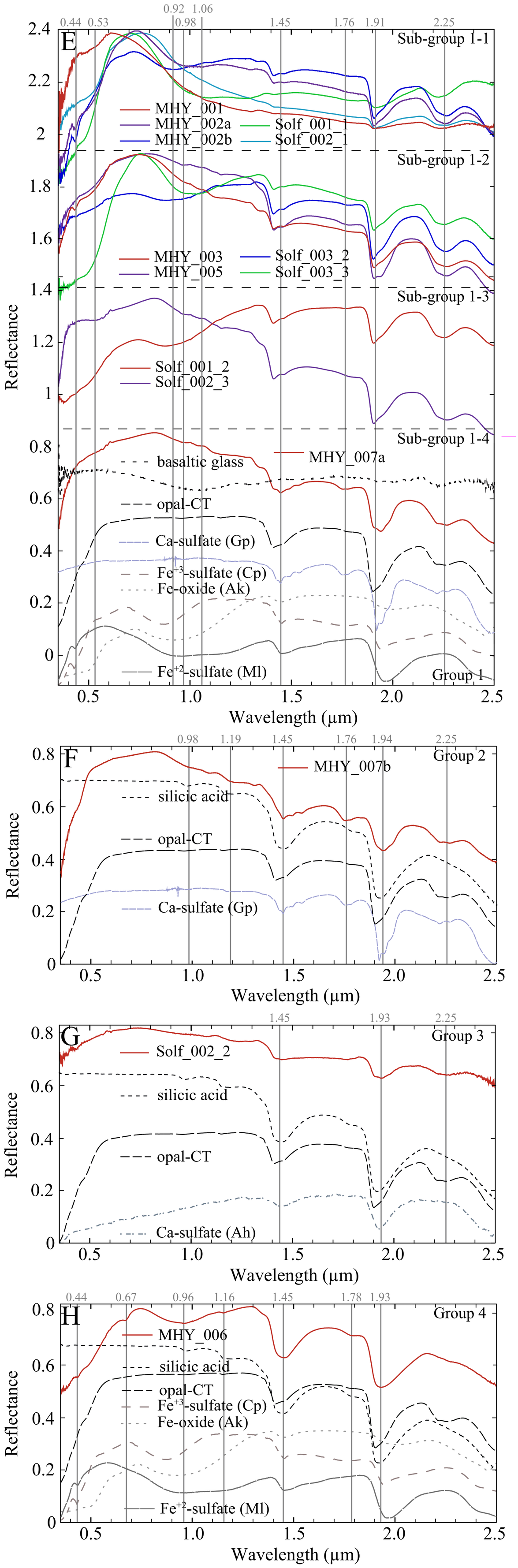

This is a preprint, the final version is subject to change, of the American Mineralogist (MSA)
Cite as Authors (Year) Title. American Mineralogist, in press.
DOI: http://dx.doi.org/10.2138/am-2018-6238

Figure 3

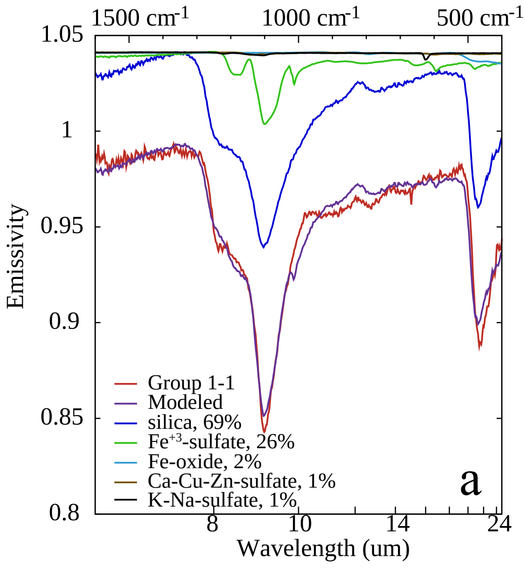

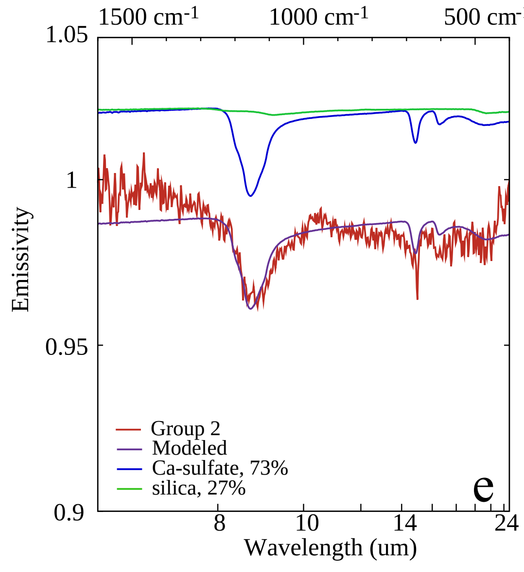

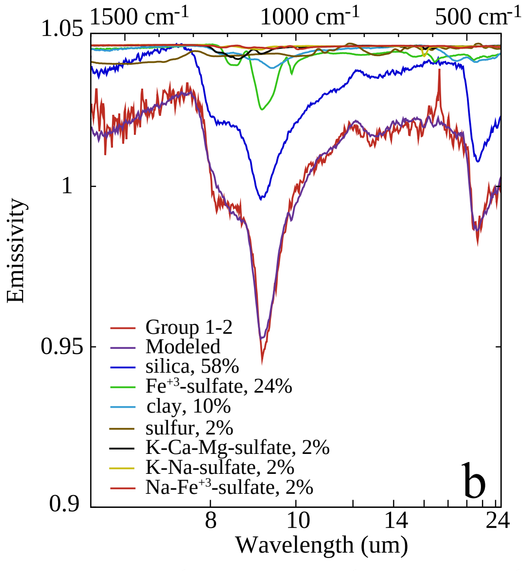

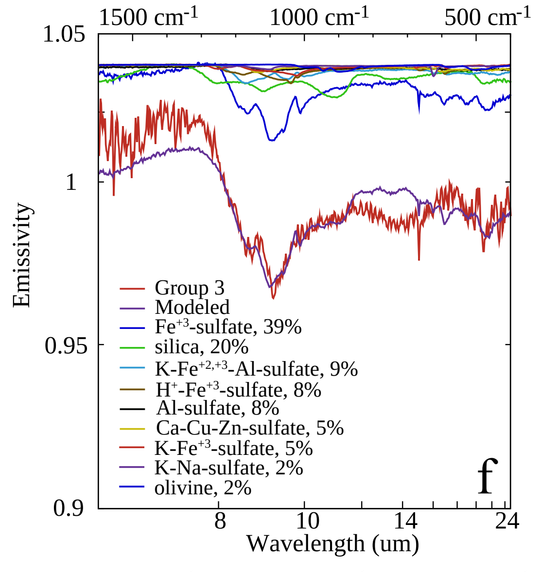

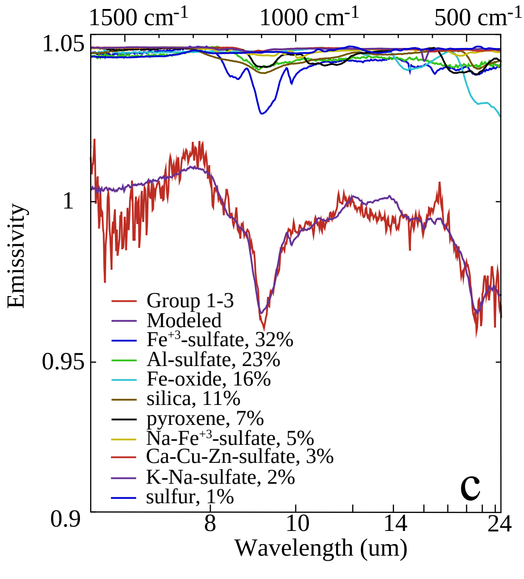

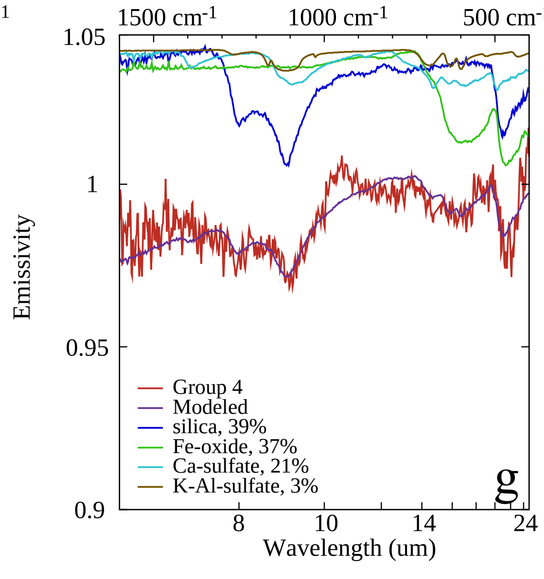

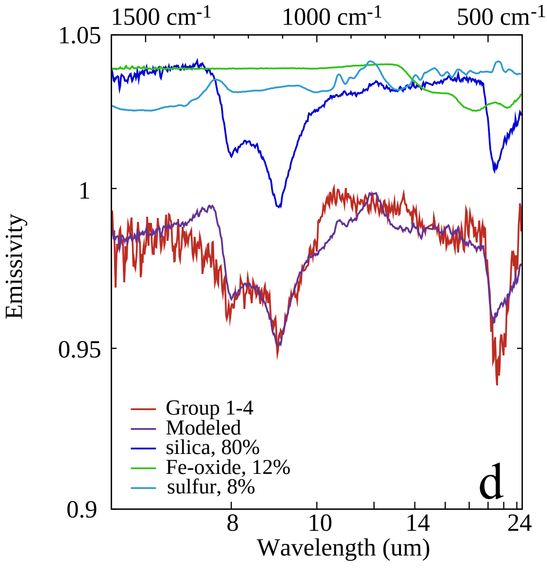

Figure 4

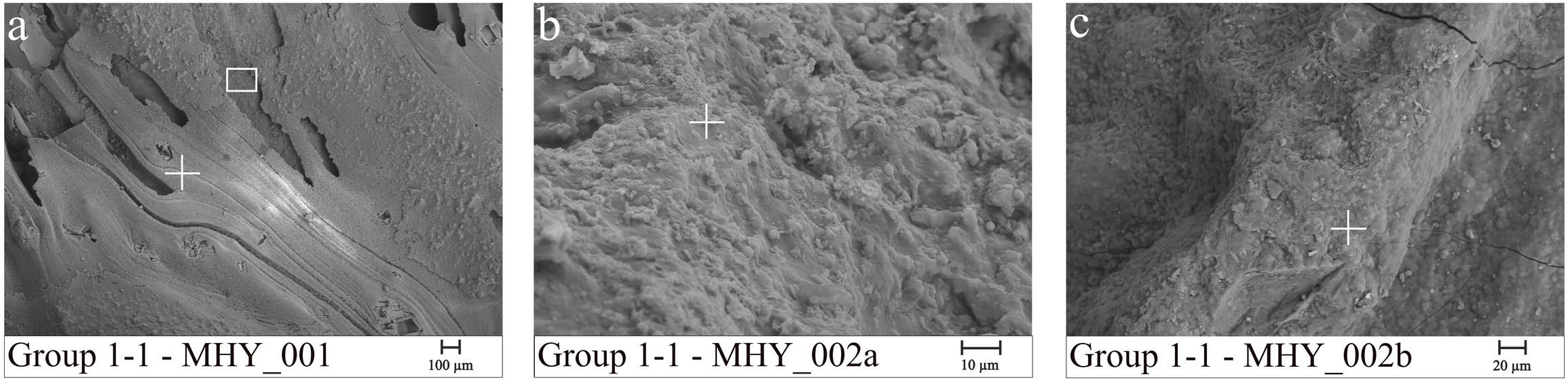

This is a preprint, the final version is subject to change, of the American Mineralogist (MSA)
Cite as Authors (Year) Title. American Mineralogist, in press.
DOI: http://dx.doi.org/10.2138/am-2018-6238

Figure 5

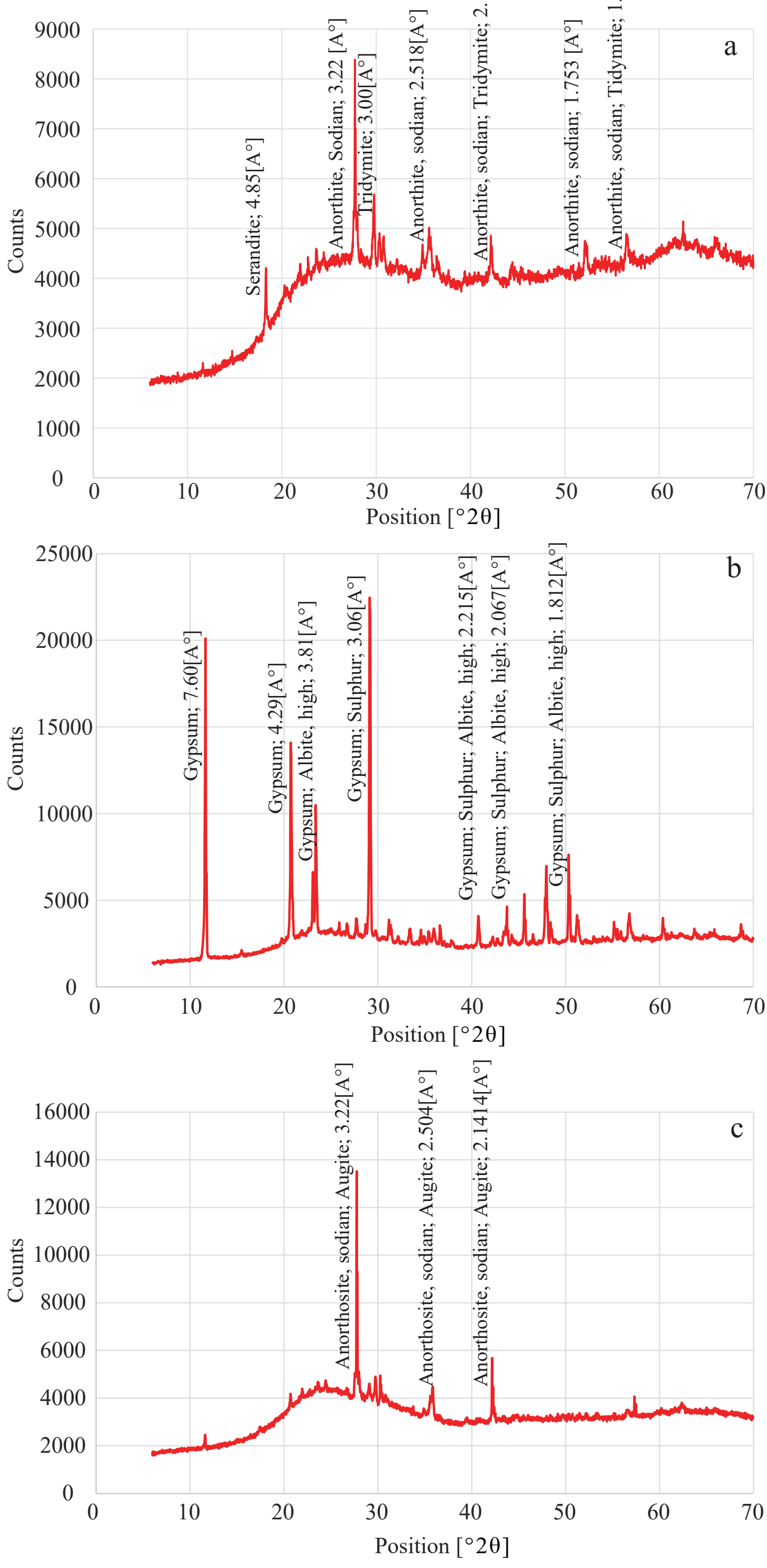

This is a preprint, the final version is subject to change, of the American Mineralogist (MSA)
Cite as Authors (Year) Title. American Mineralogist, in press.
DOI: http://dx.doi.org/10.2138/am-2018-6238

Figure 6

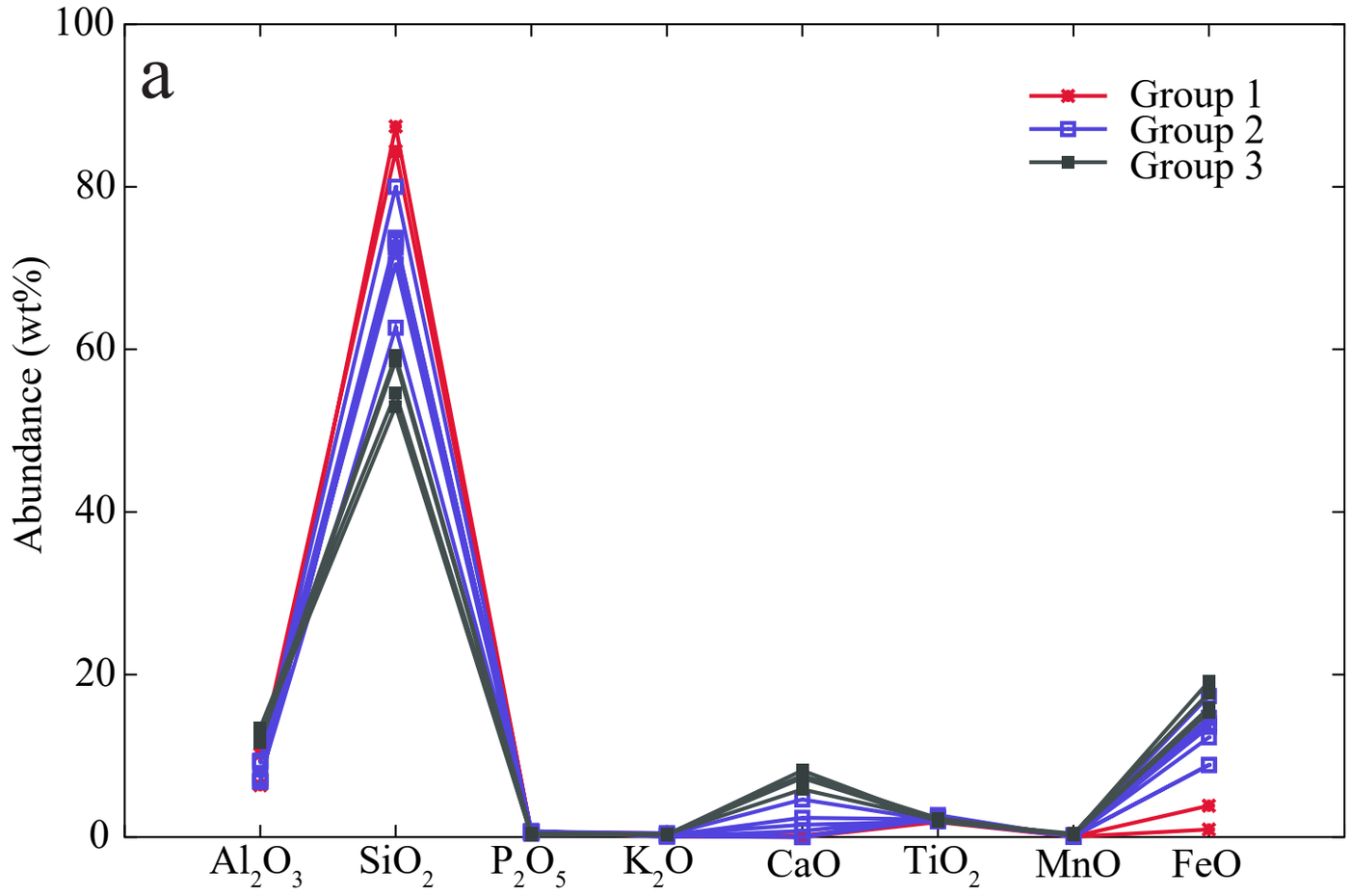

Sample Name	XRF Group	MIR Group
HI_15_Solf_002_3	1	1-3
HI_15_Solf_003_2	1	1-2
HI_15_MHY_001	2	1-1
HI_15_MHY_002b	2	1-1
HI_15_MHY_003	2	1-2
HI_15_MHY_005	2	1-2
HI_15_MHY_006	2	4
HI_15_MHY_007b	2	1-4
HI_15_Solf_003_3	2	1-2
HI_15_Solf_001_1	3	1-1
HI_15_Solf_001_2	3	1-3
HI_15_Solf_002_1	3	1-1
HI_15_Solf_002_2	3	3

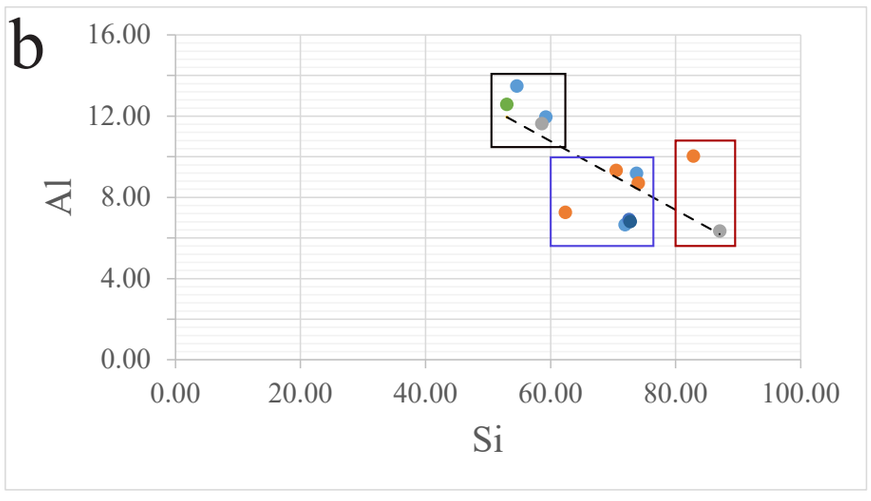

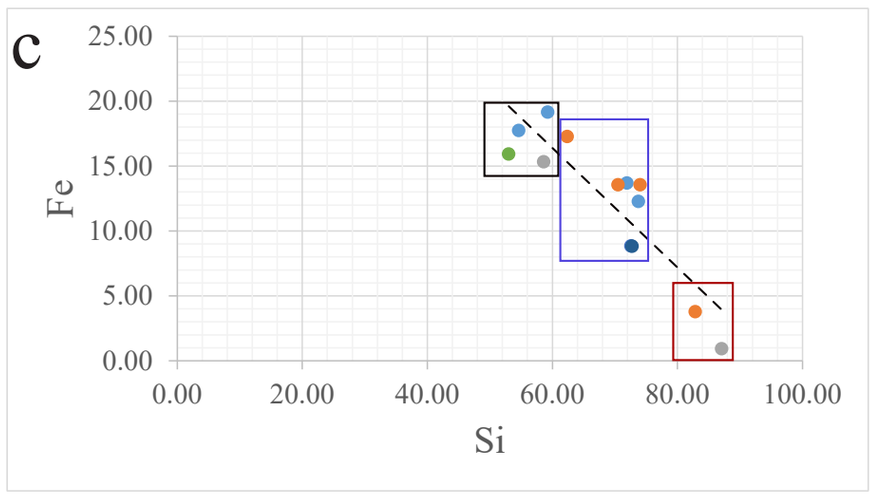

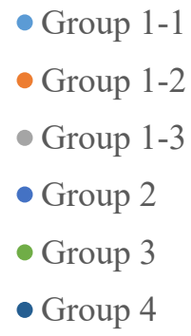

This is a preprint, the final version is subject to change, of the American Mineralogist (MSA)
Cite as Authors (Year) Title. American Mineralogist, in press.
DOI: http://dx.doi.org/10.2138/am-2018-6238

Figure 7